Report on modelling and monitoring of slow hydrology related processes for different types of the Living Labs

Deliverable 4.2 - version: v.30-03-2026

March 30, 2026

P. van der Keur, H. Müller, M. von der Thannen, H. P. Rauch, Ida Seidenfaden, Maria Ondracek, João Filipe Fragoso dos Santos, Andrei Toma, Albert Scrieciu, Miguel Potes.

REVISION HISTORY

Version	Date	Author/reviewer	notes
v.0	23-01-2026	P. van der Keur et al.	D4.2 to include LL modelling and monitoring, Bluespot analysis, adapted from 'joint paper'
v.1	27-01-2026	All D4.2 contributors	Revised title, and adjusted ToC
v.2	23-03-2026	All D4.2 contributors	First incomplete draft ready for review
v.3	27-03-2026	All D4.2 contributors	Review done and suggestions incorporated
v.4	30-03-2026	Peter v.d. Keur, Helene Müller, Ida Seidenfaden	Review comments incorporated and finalizing
v.5	31-03-2026	Miguel	Final draft submitted

Content

1 Introduction

INTERLAYER focuses on how water retention technologies can contribute to improve resilience, adaptation and mitigation to hydroclimatic extreme events while increasing water availability and quality by balancing groundwater and surface water management practices. INTERLAYER will study groundwater and surface water availability and relate it to land use (including specific agricultural practices) and water quality from a synergetic perspective so that available Slow Hydrology (SH) techniques are used in future River Basin Management Plans. To do so, we set up four Living Labs (LL) in four contrasting European watersheds to include and compare different European edaphoclimatic regions with different geologic characteristics, see Figure 1-1 and Table 1-1.

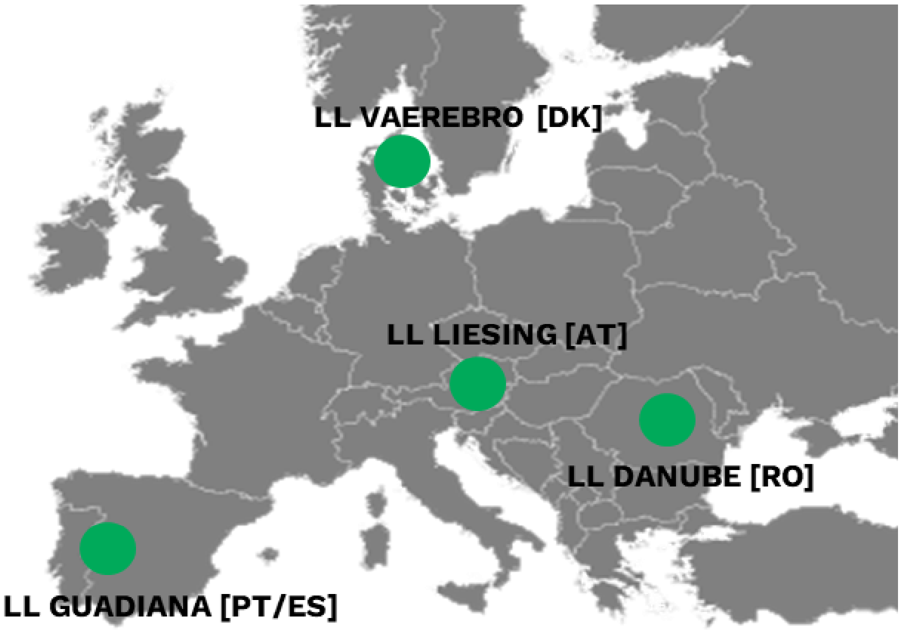

Figure 1-1 INTERLAYERs four LLs, located in contrasting watersheds in different regions of Europe (Mueller et al., D3.1)

Table 1-1 Basic properties of Living Labs river basins

	Catchment name	Area (km2)	Elevation range (m)	Annual precipitation	DTM source resolution

Austria	Liesingbach	124	156.5 - 642.8	≈501 mm	1.0 m
Denmark	Vaerebro	155	-0.2 - 59.5	≈549 mm	0.4 m
Romania	Salcia-Maglavit	775	27.2 - 350.4	≈643 mm	0.5 m
Portugal	Toutalga, Sobral da Adiça	136	143.1 - 523.0	≈515 mm	0.5 m

Vaerebro River [DK] - The about 150 km2 LL-DK including the Vaerebro river of 35 km is a heavily human-impacted basin, with a high degree of urbanization, extensive agriculture (much of it on drained land), numerous water-intensive industries, and groundwater abstraction for water supply that is close to the sustainable limit and threatened by pollution from nitrate, pesticides, and other organic micropollutants. Terrestrial nature is scattered and makes up only around 10% of the basin, and the ecological status of the Værebro River system is mostly poor, as is that of its estuary, Roskilde Fjord /1/. The area is a popular settlement, with projected population growth of about 9 % from 2025 to 2035.

Liesingbach River [AT] - The Liesingbach river is beside the Danube and the Wien river one of the main water courses in the city of Vienna. It flows 30 km through strongly populated regions in the south of Vienna. The catchment can be divided into a forest dominated area followed by an urban river section. This LL is set in a peri-urban and urban regional context, with high potential for replication due to stakeholder involvement rates (capitalized from other projects), in a region with a continental humid climate with warm summers.

Guadiana River [PT/SP] - The Guadiana river basin covers a total area of 66,800 km^2 and is shared between Spain (83%) and Portugal (17%). The Toutalga LL is a left tributary whose basin covers an area of 136 km^2, characterised by temporary watercourses and a typical Mediterranean climate. Flash floods and long periods of drought are two of the main hydrological risks in a river basin where more than 95% of land use is devoted to agricultural and forestry systems. In the last WFD assessment cycle, surface waters achieved good and reasonable chemical and ecological status, respectively, while groundwater showed poor chemical and quantitative status. The village of Sobral da Adiça, the only urban area with 1,000 inhabitants, is mainly supplied by groundwater from the Moura-Ficalho aquifer, so enhanced integrated management of surface and groundwater will yield significant gains in terms of climate resilience and ecological benefits. The LL allows for a source-to-sea approach.

Danube River [RO] - A stretch of the former floodplain of the Danube River, between Salcia and Maglavit villages consisting of 200 ha along the corridor at Salcia, with abandoned fish farm, arable land with mix uses, including planted forest and pasture. This LL is set up in a continental humid with a hot summer climate. The area has high potential for improvement of lateral connectivity through Nature-based solutions (NBS) implementation in order to re-connect the surface and groundwater to increase resilience and reduce the impact of drought.

As the LLs are located in different and contrasting European regions, they show different processes and settings in the landscape as well as various microclimatic, hydrological and geological characteristics. The present document describes methodologies for parameterization of hydrologic processes for retaining surface water for recharge to shallow groundwater for water storage and various purposes described for each Living Lab above. Additionally water quality aspects were included. Parametizations are implemented in applied hydrological models and monitoring schemes.

.

2 Hydrologic processes, modelling and monitoring in four Living Labs

2.1 Hydrological modelling / monitoring Liesingbach river catchment

River Liesingbach is challenged by both hydroclimatic extremes: Low flow and floods. In connection with restoration efforts in the corridor the hydrological system is slowed down during dry periods. Leading to higher residence times, longer exposure to energy input through radiation and therefore higher water temperatures, which put the river's ecology at risk during drought periods. The main challenge for the river Liesingbach is summer drought and elevated temperatures, which put the river's ecology at risk. Regarding the opposite hydroclimatic extreme, for current climate a 100 years flood protection exists. Even if precipitation patterns change under climate change, the system should be able to remain at this protection level. The idea is twofold: to ensure future flood protection by introducing Slow Hydrology measures upstream that might also ensure slow release (e.g. over one week) over low flow periods, and to provide more shade to improve the energy balance by reducing incoming radiation.

Therefore, two different modelling approaches are applied to the Living Lab, see Figure 2-1. In the upper catchment a rainfall-runoff model is set up with its outlet at the gauging station Paul-Katzberger-Gasse (Figure 2-2). In the urban catchment low flow situations are considered in a water temperature model.

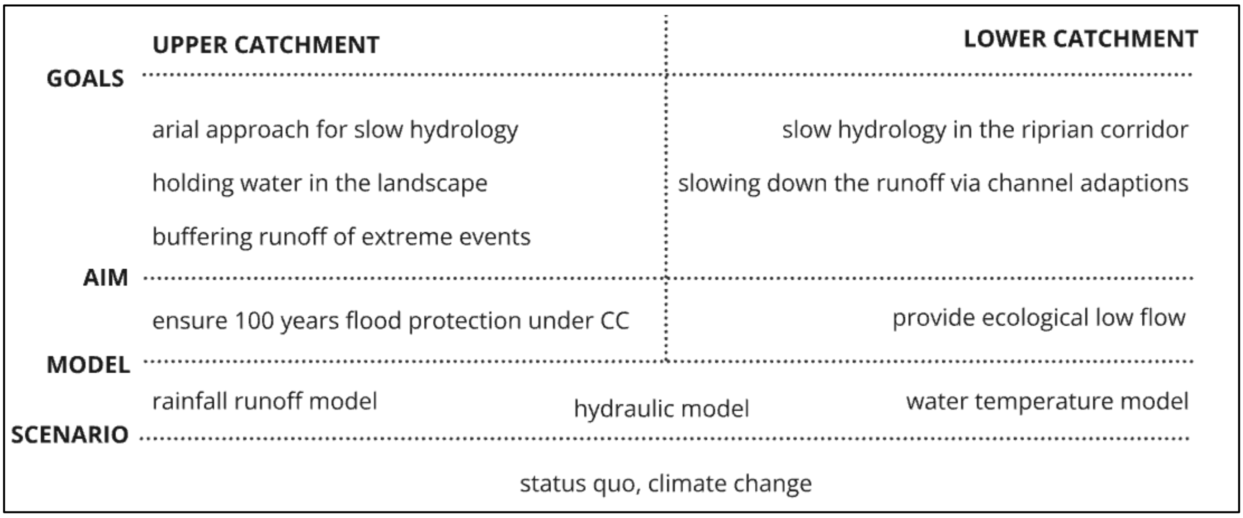

Figure 2-1: Twofold modeling approach divided in upper and lower catchment of the Liesingbach river.

Monitoring efforts within the Liesingbach river catchment are diverse and cover meteorological parameters, discharge and water levels, water temperature and groundwater levels, see Figure 2-2. Meteorological data is observed in different temporal resolutions from Geosphere Austria. Responsibility of the hydrological and groundwater data as well as long term water temperature is by the City of Vienna, MA 45 Wiener Gewässer, department of Hydrology. Short term water temperature measurements were carried out through the EU Project Life EnCAM.

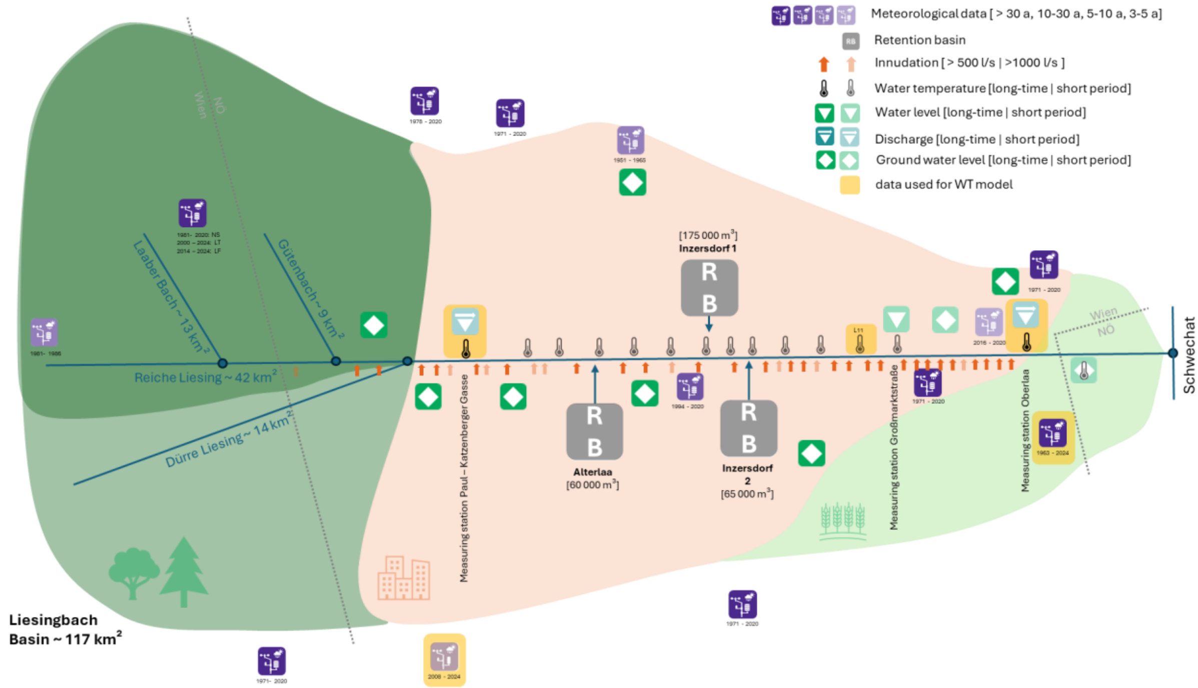

Figure 2-2: Sketch of LL Liesingbach including monitoring stations. Observation points marked in yellow were used for modelling

2.1.1 Water Temperature Model

2.1.1.1 Model Setup

The water temperature was modeled using the HEC-RAS water quality toolbox. For the hydraulic calculations, the 1D energy equation was solved via the standard step method for steady flow conditions. For water temperature simulation, the full energy budget method was applied. The model solves a one-dimensional advection-dispersion equation with additional terms accounting for lateral inflow, solar radiation, and heat exchange with the atmosphere and streambed (Figure 2-3) (Zhang and Johnson, 2017). This method uses source and sink terms to describe the net effect of all heat inputs (sources) and heat losses (sinks) on the water temperature within each computational cell (Brunner, 2016; Zhang and Johnson, 2017). Heat sources and sinks are primarily dependent on the net heat flux (Figure 2-4). Calibration was carried out via adjusting the default parameters of the full energy budget method were adjusted, including the wind function and sediment-dependent parameters.

$$\frac{\partial}{\partial t}(VT_w) = -\frac{\partial}{\partial x}(QT_w)\Delta x + \frac{\partial}{\partial x}\left(AD_x\frac{\partial T_w}{\partial x}\right)\Delta x + S_L + S$$

where

V = volume of the computational cell (m^3)
T_w = water temperature (°C)
t = time (s)
Q = flow rate ($m^3\ s^{-1}$)
A = channel cross-sectional area (m^2)
x = distance along channel (m)
Δx = distance between cross sections (m)
Dx = dispersion coefficient ($m^2\ s^{-1}$)
S_L = source/sink term representing the time rate of inflow heat exchange (°C $m^3\ s^{-1}$)
S = source/sink term representing the time rate of change of local external heat exchange (°C $m^3\ s^{-1}$).

Figure 2-3 1D heat advection-dispersion equation used for water temperature modelling

For heat transport the source/sink term is

$$\text{Heat}_{\text{Source/Sink}} = \frac{q_{net}}{\rho_w C_{pw}}\frac{A_s}{V} \qquad (19\text{-}24)$$

q_{net} = net heat flux at the air water interface (W m^{-2})
ρ_w = density of water (kg m^{-3})
C_{pw} = specific heat of water (J kg^{-1} C^{-1})
A_s = surface area of water quality cell (m^2)
V = volume of water quality cell (m^3)

Net Heat Flux

Net heat flux is computed as the sum of individual heat budget components:

$$q_{net} = q_{sw} + q_{atm} - q_b + q_h - q_\ell \qquad (19\text{-}25)$$

q_{sw} = solar radiation (W m^{-2})
q_{atm} = atmospheric (downwelling) longwave radiation (W m^{-2})
q_b = back (upwelling) longwave radiation (W m^{-2})
q_h = sensible heat (W m^{-2})
q_l = latent heat (W m^{-2})

Figure 2-4 Calculation of the source/sink term for heat transport and the net heat flux in HEC-RAS

2.1.2 Input data and boundary conditions

2.1.2.1 Geometry

A uniform trapezoidal cross-section derived from unrestored river stretches was used, with a stream bed width of 4 m and bank slopes of 1:3. The modeled river section extends from gauge Paul-Katzbergergasse to gauge Oberlaa (Figure 2-2), covering a length of 8.3 km with a longitudinal slope of 0.005. For model calibration and validation, the simulated water temperature at the location of Logger 11 was compared with observed measurements. Manning's roughness coefficients were set to n = 0.022 for the riverbed and n = 0.033 for the riverbanks.

2.1.2.2 Hydraulic Inputs

The discharge for the hydraulic setup was set to 0.11 m^3/s, representing the median flow from the 10-year representative hot periods (RHPs) dataset.

2.1.2.3 Vegetation Inputs

The characterization of riparian vegetation was conducted using hemispherical photography. Photographs were taken every 500 m directly above the water surface in the middle of the channel. Additional images were captured at locations with significant changes in vegetation cover. In total, 94 images were acquired on 06.09.2024 along an approximately 18 km section, resulting in a density of 5.2 photos/km. A Canon EOS 60D with a Sigma EX DC 4.5 mm fisheye lens mounted on a self-leveling camera mount was used for image acquisition.

Solar radiation indices and canopy indices were derived from the processed photographs using HEMIVIEW software (Delta-T Devices Ltd., 1999). Calculations were performed using the simplified atmospheric radiation model (Default Simple Model), and images were analyzed using the threshold method. Gap fraction for the sunmap was calculated by cross-referencing gap fraction with solar tracks (Rich *et al.*, 1999). The gap fraction represents the ratio of visible sky within a sky sector, where sectors are defined by solar tracks, time of day, and day of the year. Direct solar radiation was derived by multiplying the gap fraction of each sector with the radiation from that sector (Rich *et al.*, 1999). Direct solar radiation (MJ/m^2) was calculated with a temporal resolution of 15 minutes for diurnal curves. The model accounts for transmission and scattering by the earth's atmosphere, while reflection effects are not considered. Pixels classified as vegetation were assumed to be completely opaque to light. Calibration coefficients were set according to the lens specifications. The location was set to 48.12° N, 16.28° E, 200 m a.s.l., with a magnetic declination of 3.8° E.

For modeling scenarios with realistic solar radiation conditions, daily patterns were derived from the mean curves of photographs averaged over 500 m intervals. This spatially distributed approach captures the natural variation in riparian vegetation along the stream corridor. In addition to the spatially variable scenario, constant vegetation scenarios at different density levels were developed. For this purpose, characteristic vegetation conditions were identified based on direct solar radiation below canopy on a day in July at the 10th, 25th, 50th, 75th, and 90th percentiles, representing high to low vegetation density, respectively.

2.1.2.4 Hydroclimatic Inputs

The meteorological dataset for 5820 (N 48.10694, E 16.27000) and 5917 (N 48.12500, E 16.41944) (GeoSphere Austria, 2024) was used. The meteorological dataset from both measurement stations within a 30 min dataset from 2015 to 2024 was scanned for riparian heat periods. Based on a previous conducted driver analysis the river heat period (RHP) was defined as a consecutive timeframe of seven days within each year, that shows the maximum in the mean air temperature, the maximum in the sum of global radiation and sunshine duration. As boundary condition the sum of precipitation was set to minimum, in order to select only timeframes with stationary hydraulic conditions. This was a requirement for the subsequently conducted modelling. For each year one RHP was selected by the detection tool, see Figure 2-5.

$$RHPI_i = Z(\overline{T}_i) + Z(G_i) + Z(H_i) - Z(R_i)$$

$$Z(x) = \frac{x - \mu_x}{\sigma_x}$$

$$i^* = \arg\max_i RHPI_i$$

$RHPI_i$ ... *river heat period index*
$\overline{T}_i$ ... *mean temperature over 7 days*
G_i ... *cumulative global radiation over 7 days*
H_i ... *cumulative sunshine duration over 7 days*
R_i ... *cumulative precipitation over 7 days*
Z ... *standardized function*
μ_x ... mean
σ_x ... standard deviation

Figure 2-5 Detection function for yearly 7 days river heat period

Each variable is transformed into a standardized score. All scores are combined into the river heat period index (RHPI). For each year the period with the highest RHPI was selected. The detection was carried out based on 30 min data for meteorological station w5820. Based on the dataset median values of all detected RHPs are calculated and additional hydro climatic parameters were extracted from (GeoSphere Austria, 2024) dataset. The median RHP is used as model input, see Figure 2-6.

Water temperature data was provided by the city of Vienna, MA45 Wiener Gewässer in hourly resolution. The dataset was transformed into 30 min data by linear interpolation.

For future projections climate data from D4.1 was used. Based on the meteorological water balance three scenarios (10%, 50% and 90% percentile) were selected. RHPS were detected analogue to historical data and grouped into two time periods: 2026-2065 and 2071-2100.

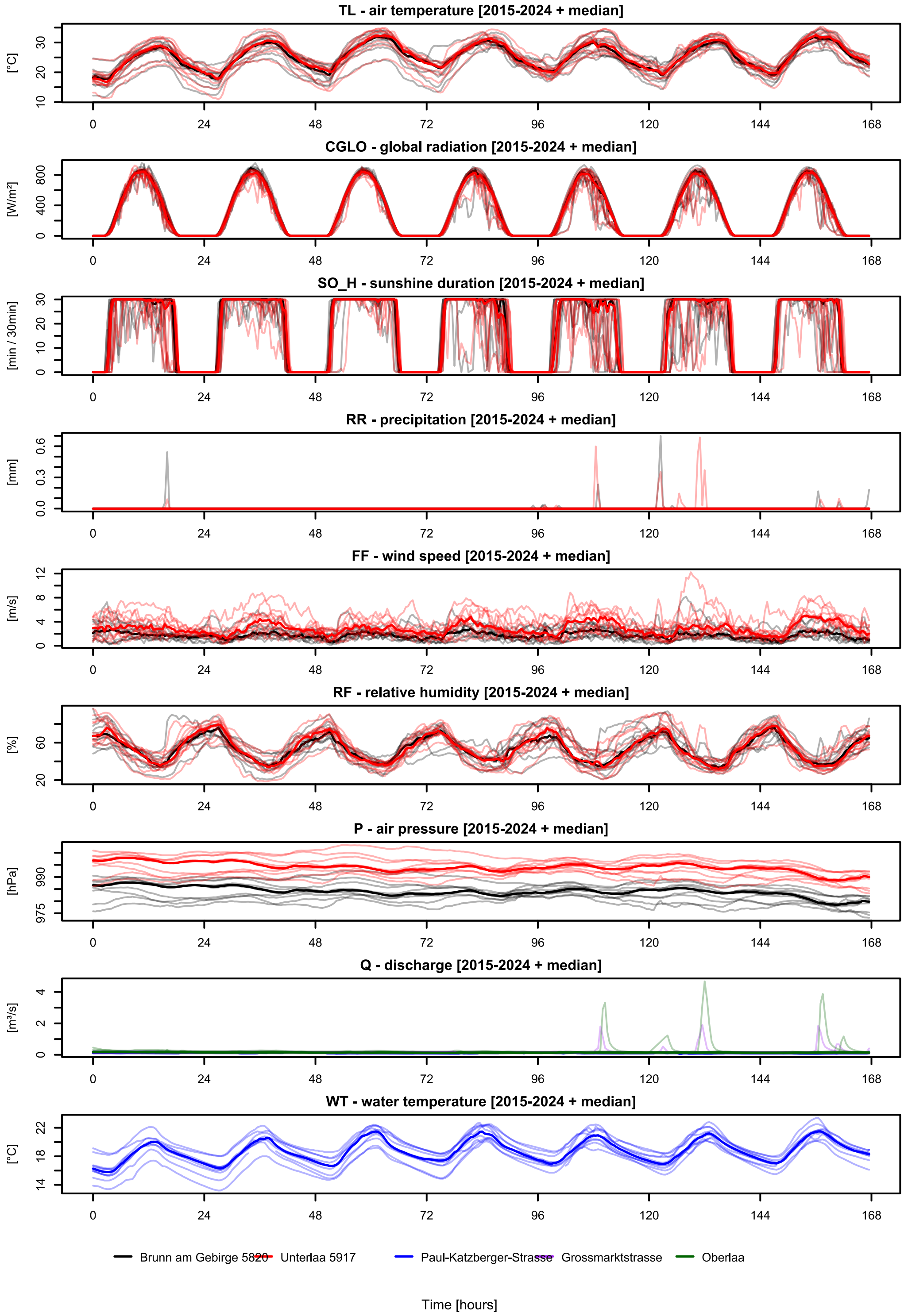

Figure 2-6: Detected River Heat Periods (RHP) within 2015-2024. Median curves (bold lines) function as model input for the water temperature model.

2.1.2.5 Water Temperature Model Inputs

The upstream boundary condition for water temperature was defined using measurements from gauge Paul-Katzbergergasse. Suspended sediment concentration was assumed to be 20 mg/L, with sediment temperature equal to the mean annual air temperature.

Meteorological input data were derived from the 10-year RHPs dataset. Since HEC-RAS does not explicitly account for riparian shading, the reduction in energy input was incorporated through adjusted shortwave radiation values (Stonewall and Buccola, 2015). In this study, shading effects were quantified using radiation inputs calculated from hemispherical photographs, see Vegetation Inputs.

The model was calibrated using data from 2022 and validated using data from 2021. Calibration was carried out over the wind function and sediment parameters. Calibration parameters are listed in Figure 2-7

wind_a	Coefficient a in wind function	unitless	1
wind_b	Coefficient b in wind function	unitless	5
wind_c	Coefficient c in wind function	unitless	4.6
wind_kh_kw	Diffusivity ratio	unitless	0.75
h2	Sediment layer thickness	m	0.25
pb	Sediment bulk density	kg/m^3	1850
Cps	Sediment specific heat	J/kg/K	2200
alphas	Sediment thermal diffusivity	m^2/d	0.2

Figure 2-7: Calibration parameters water temperature model

Groundwater inflow was considered negligible at the study site due to the predominantly sealed riverbed. Surface water inflow was not expected during RHPs.

Model scenarios cover different projections periods, climate change pathways and vary within their vegetational cover. An overview is given in Figure 2-8.

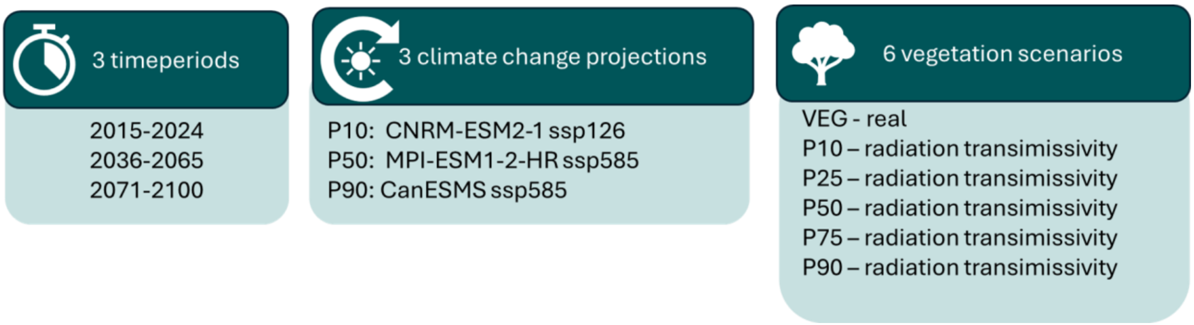

Figure 2-8: Model scenarios in LL Liesingbach

2.2 Hydrological modelling / monitoring Vaerebro River catchment

The overall aim is to handle hydrological extremes now and in a changing climate, specifically by delaying water during extreme wet conditions and storing it for dry periods. The hydrological modelling for Værebro catchment is based on a submodel of the National Hydrological model of Denmark (DK-Model), that describes both the natural hydrological cycle such as evaporation, soils, streams and groundwater interactions and human impacts from wastewater, abstraction and irrigation. The submodel is used for locally assessing water retention solutions and slow hydrology interventions, through different modelling scenarios.

2.2.1 Integrated hydrological model

The submodel covers Værebro catchment, that is situated on the island of Zealand in the eastern part of Denmark, Figure 2-9. The catchment is 154 km2, and the draining river (Værebro Aa) runs from the east to the west and enters the fjord of Roskilde that is connected to Kattegat.

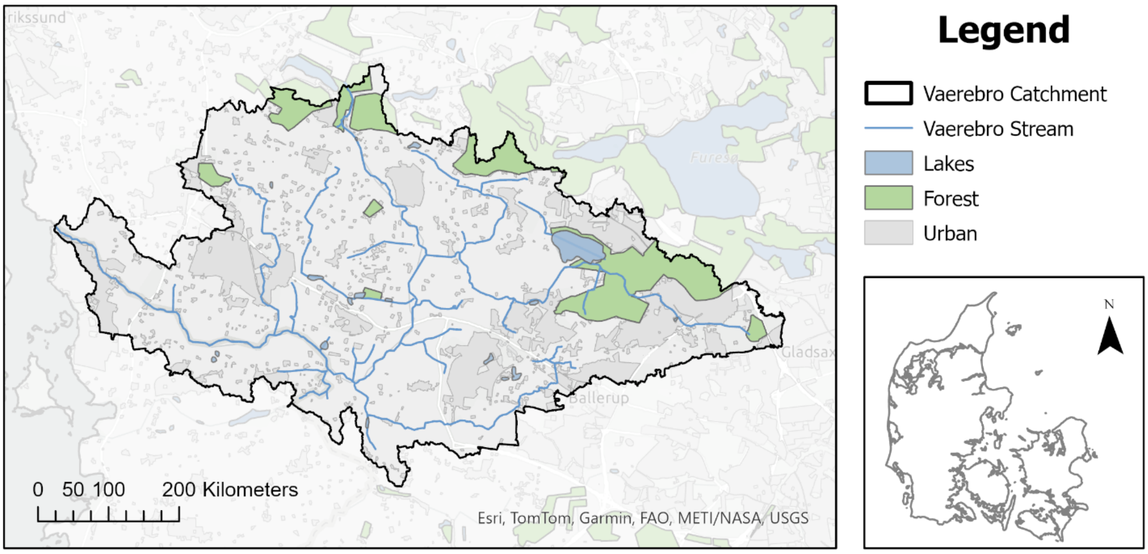

Figure 2-9 Map of the Danish Living Lab Værebro submodel location.

2.2.1.1 Model setup

The submodel integrates 3D groundwater flow with surface water processes, root zone dynamics, overland flow, and river routing. It operates on grid resolutions of 100 m and is built using the MIKE SHE (Abbott et al., 1986) and MIKE HYDRO modeling frameworks generated by DHI (DHI, 2020), see concept figure, Figure 2-10.

The Værebro model has been improved with several local adaptations including in-stream topographic data (cross sections), additional observations (water levels in Værebro River, newer groundwater measurements in the catchment area), and an upgrade to a more advanced river flow calculation module (Hydrodynamic).

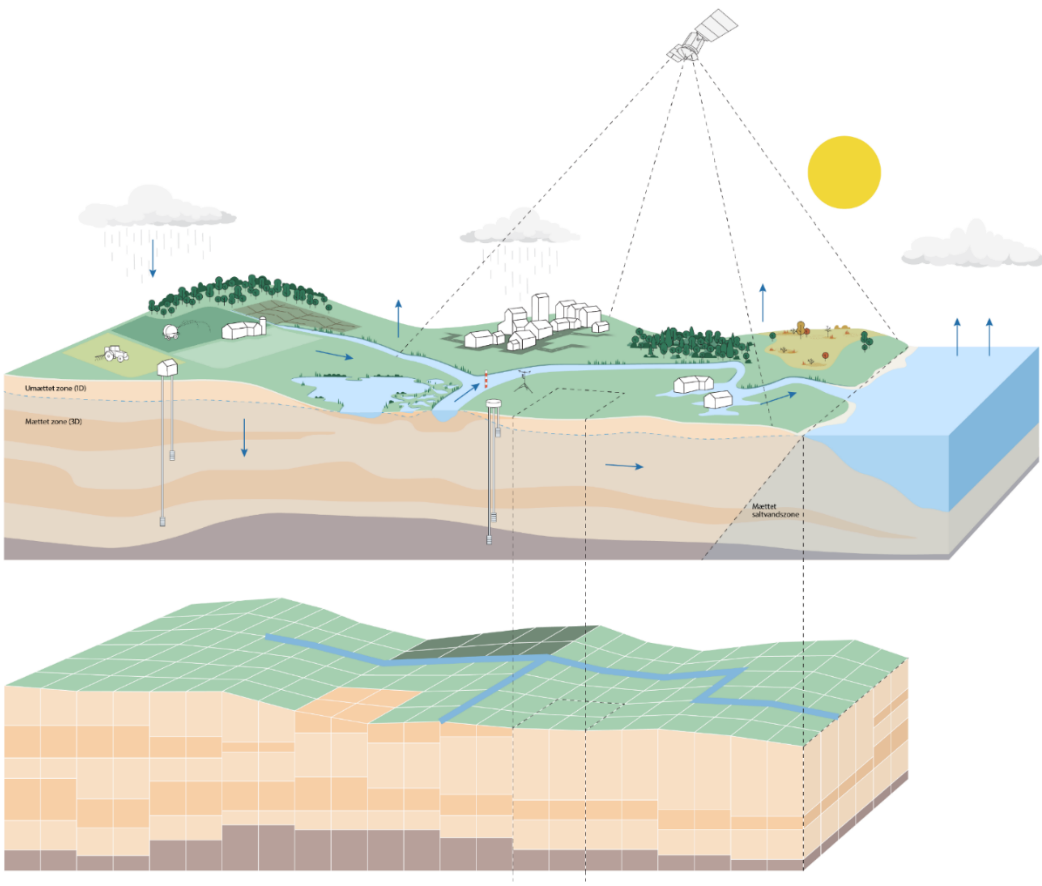

Figure 2-10 Illustrative overview of the principles behind the DK-model.

2.2.1.2 Input data and boundary conditions

The input data to the model is quite substantial and consists of 1) climatic forcing, 2) landscape maps, 3) geology and 4) anthropogenic pressures e.g. from reported water use and wastewater. For a detailed introduction to the datasets and their pre-processing please refer to Henriksen et al. (2021 and Stisen et al. (2019).

The climatic forcing consists of a gridded precipitation data set from the Danish Meteorological Institute (DMI), where precipitation station data have been gridded to a 10 km grid resolution (DMI, n.d.; Scharling, 1999). The precipitation data has been corrected for undercatch using a dynamic approach (Stisen et al., 2012). Similarly, the temperature is a 20 km grid product from DMI, while the potential evapotranspiration is calculated using a modified Makkink formula (Scharling, 2001) in a 20 km grid.

The map of the landscape consists of a land use, and soil map. The land use maps primary function in the model, is to describe the root zone (root development and depth) and the leaf area index, that both are major controls on the evapotranspiration calculation. These two variables are determined from satellite data where a climatology is developed for each month of the year for every grid in the model. The variables are thus not connected to a specific category of land use but rather an expression of the long-term vegetation in the specific grid. Related vegetation properties are calculated based on these two variables on a grid basis following the approach of (Soltani et al., 2021). The soil maps are based on the official soil type maps from (Jakobsen og Tougaard 2020) and (Pedersen, et al. 2011/19). Soil types with limited extent are grouped with soil types of similar properties, resulting in a total of nine different soil categories in the model.

The geological model is based on the common public hydrogeological model, called FOHM (MST, 2021), (Arvidsen, et al. 2020). The model consists of a 2D description of major hydrostrati-graphical units, their depth, thickness, connectivity and properties.

The anthropogenic pressures consist of reported groundwater abstractions from the water supply (drinking water, and industry), and wastewater discharges to specified locations on streams and rivers as found in the National Well database, Jupiter (GEUS, 2024).

The Værebro model is generated as a stand-alone submodel, with dynamic boundary conditions from its parent, the DK-model, in order to accommodate transboundary groundwater flow.

2.2.2 Monitoring data

The model's ability to represent reality presented as differences between simulated heads, discharge and water level in Værebro compared with observations. The parent model was calibrated for the period of 2000-2010, statistics on the model performance will therefore be presented for this period. However, to evaluate the performance of the model on a more recent time period, additional data for the period of 2020 – 2023, has been included. Due to the simple representation of the stream flow (routing) the water levels where not traditionally part of the calibration of the DK-model but are included here to evaluate the performance of the full hydrodynamic solution implemented in the Værebro model.

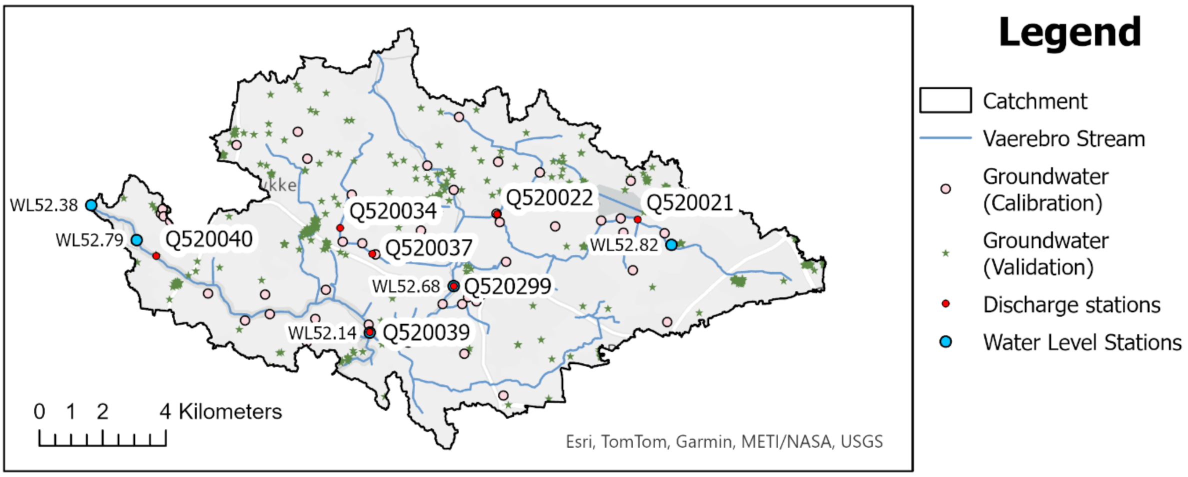

Figure 2-11 Map of the location of observations.

Figure 2-11 shows the location of observation points in the DK-LL for groundwater level and discharge. The original DK-model was calibrated for the period of 2000-2010 (Stisen et al., 2019). The Værebro model, therefore, utilizes the same data but supplemented with more recent data for evaluation of the sub-model's performance. The figure shows both discharge (7 stations), stream water level (5 stations), and groundwater levels (53 stations).

Of the seven discharge stations, four of them were used in the calibration as they have data in 2000-2010, of these, two stations cover the entire calibration span (Q520022 and Q520039). The final two only have data in the recent years and are thus only used for validation (Q520040 and Q520299).

2.2.3 Scenarios

To investigate the potential impact of slow hydrology compared to the impact from anthropogenic decisions in the catchment, the hydrological model is run with two slow hydrology scenarios and three anthropogenic scenarios (Table 2-1). The slow hydrology scenarios tested so far are the Afforestation and No Drainage scenarios.

The afforestation scenarios are linked to decisions in the new governmental state agreement, the Green Tripartite, to increase the forested area in Denmark. The benefits from the different scenarios in relation to the Green Tripartite are also included in Table 2-1. This agreement was formed with the purpose of decreasing nitrogen loads to surface water and the ocean, as well as reaching climate reduction goals for wetting of lowland and peat areas. An additional point was to increase biodiversity in the open land. For Værebro, there is at present planned an increase in forested areas by 20%. The afforestation scenarios represent this potential future.

The No Drainage scenario is a synthetic scenario to test the new flow paths and water balance, resulting from a landscape without drains. As a part of the Green Tripartite, one of the measures is cutting of drains during rewetting and for retention, the scenario tests catchment response to this measure; however, in a very broad manner, as all drains are removed in the model.

The two anthropogenic scenarios are based on potential increases in groundwater abstraction in the area (-50% or +100%). Representing the unknown future abstraction pattern in the area, population growth (especially in Copenhagen) could indicate a preference for a high abstraction rate, whereas pollution-related risks could indicate the closure or relocation of high-yield groundwater wells in the area. The third anthropogenic scenario represents the municipalities' plan to relocate the local small wastewater treatment plant, which discharges to small stream systems, to the seaside, thereby eliminating inflow to several discharge points in the river network.

Table 2-1 Table of scenarios and relevant co-benefits

Scenarioes		(Co-)benefits for the Green Tripartite			(Co-)benefits for drinking water resources
		Biodiversity	GHG	Nitrate	
Slow hydrol	Afforestration + 20 %	+	+	+	?
	No drainage	+	+/-	+	+
Anthropogenic	Waste water scenario	+/-	?	+/-	nn
	Abstraction: -50%	+	+	?	+
	Abstraction: +100%	-	?	?	-

2.3 Hydrological modelling / monitoring Toutalga River catchment

2.3.1 Coupled monitoring–modeling demonstrator

The benefits of slowing down hydrological processes within a watershed dominated by intermittent rivers and ephemeral streams are very common in Mediterranean regions, where urban agglomerations are exposed to extreme events such as droughts and floods. Slowing down hydrological processes allows for an integrated response, enabling the protection of people and property while creating strategic water bodies that contribute to ecological support, animal watering, and aquifer recharge.

Since extreme hydrological events are increasing in frequency and intensity, particularly in this region, where much of this trend is exacerbated by climate change, it highlighted the need for integrated, local-scale observational and modelling approaches capable of supporting adaptation and risk-reduction strategies by considering detention and retention systems on a pristine basin as the Toutalga pilot basin, where the streamflow regime is non-regulated.

A comprehensive approach combining on-site meteorological and hydrological monitoring, GIS-based catchment characterisation and hydrological modelling to assess extreme precipitation and coupled runoff processes in the Toutalga was implemented as a living demonstrator. The established monitoring network (Figure 29) provided high-quality input and validation data for hydrological analysis, and it considered an autonomous, real-time transmission, fully operational meteorological station used to assist the HOBO's water level pressure transducers to ensure measurement quality. HOBO's were installed on the outlet riverbed (38.050867° N, 7.245054° W) of the two main sub-basins (Rib. Toutalga and Rib. S. Pedro) for measuring the barometric pressure and water temperature with a frequency of 5 minutes. The meteorological forcing, to be included in the hydrological model, considered a 5 min precipitation records taken from the SNIRH (National Water Resources Information System) meteorological station, located at the center of the basin (38.017630140° N, -7.26051415° W). Grid-based precipitation data were not included due to the unavailability of datasets with sufficient resolution to adequately cover the basin.

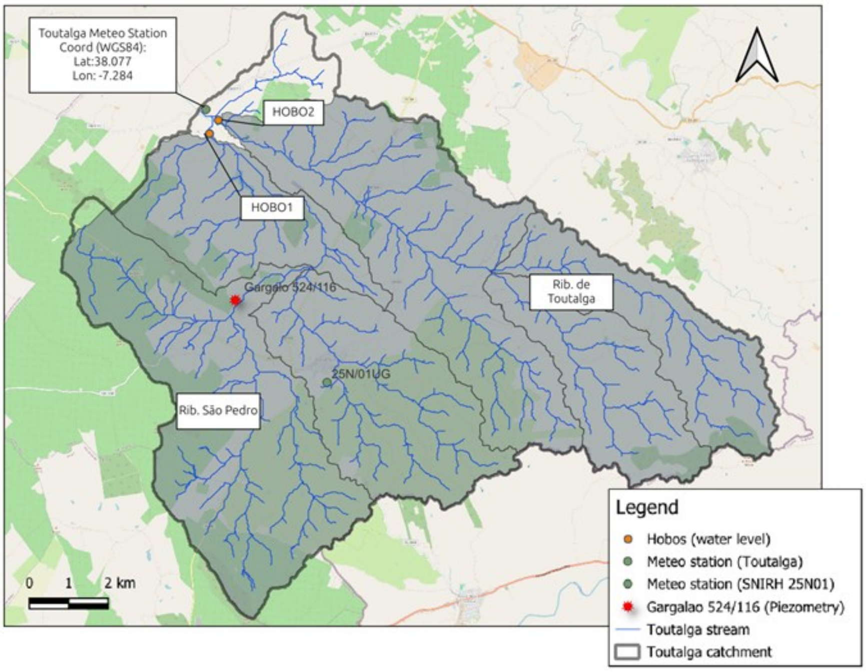

Figure 2-12 Location of the monitoring system considered

Water-level time series were used to derive site-specific stage–discharge curves, synthetically constructed based on field-observed irregular channel geometry / hydraulic characteristics (area and wetted perimeter) and the Manning's formula, see Figure 210 below. The resulting discharge series were tested and used as observed flow data for hydrological model calibration and validation.

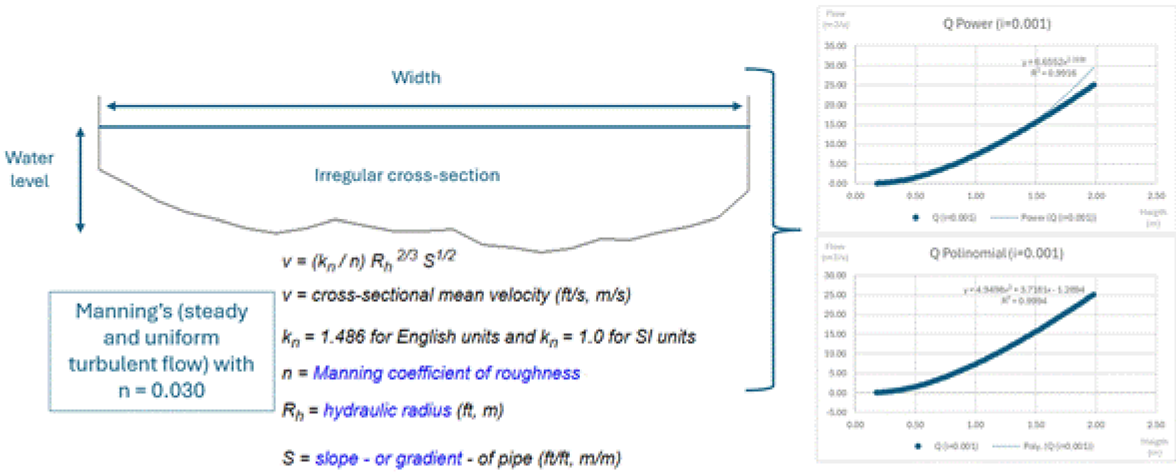

Figure 2-13 Syntethic rating curves tested on the hydrological model.

Comprehensive GIS-based basin characterization was conducted using a 0.5 m high-resolution Digital Elevation Model (DEM), which was resampled to a 10 m resolution to reduce small-scale elevation noise, in conjunction with land use/land cover datasets. The workflow included DEM-driven basin and sub-catchment delineation, stream network extraction and validation against military topographic maps, slope and land use analysis.

2.3.1.1 Hydrological model setup

The lumped Hydrological model was developed via HEC-HMS, considering an event-based approach. The SCS Curve Number method was considered for loss estimation with the area-weighted Curve Number (CN) values obtained under wet antecedent moisture conditions (AMC III) to better capture soil moisture responses (Jaafar *et. al.*, 2019). The SCS unit hydrograph for runoff transformation, and Muskingum routing for channel flow propagation. The models were developed, calibrated, and validated for both Toutalga and São Pedro basins using flow observations from 12/2024 to 11/2025, with the highest flow events selected as representative extremes.

2.3.1.2 Pond design - Hydraulic model

Urban flood protection against extreme precipitation events is also a challenge the Toutalga basin is facing. In Sobral da Adiça village flood events has been occurring more frequently in the last decades as part of the geomorphological characteristics of the area as well as changes in the extreme precipitation patterns that lead to flash floods with social, economical and ecological impacts. Within this project some restoration efforts were projected over the existent urban drainage system to fulfil a dual purpose of flood protection by temporary water detention and surface storage of water volumes to encourage the maintenance of ecological status. This is achieved by modelling the urban drainage system for two scenarios, one for the 100 year flood event over the existent urban drainage system, in order to evaluate its actual conveyance capacity and the other with two ponds implemented upstream of the village, both using the most up to date precipitation data from the near observational ground meteorological station with long records of data.

The design storm intensity was the 100 years event with the same duration of the time of concentration of each pond subbasin taken from the maximum annual daily precipitation (MADP) series of the Amareleja station (IPMA, ID 250) with coordinates (38.21668531° N, -

7.21668292 ° W). The design criteria attended to the fast hydrological response of the basin as well as the common design rules applied in Portugal.

The MADP series for the period from 1963 to 2024 were best fitted to a log-normal distribution using the maximum likelihood method, yielding a value of 72.9 mm for a probability of 0.990 (100-year return period). The IDF of Beja (27G/01) from SNIRH was used to convert the daily precipitation into a design event with the same duration of the time of concentration of both pond sub basins, resulting in 59,5 mm and 61,6 mm for pond 1 and pond 2, respectively (Figure 2-11). The hydrological modelling was performed using HEC-HMS, applying the SCS Curve Number method as the loss method, unit hydrograph transformation, and Muskingum routing for channel flow propagation with basin characteristics extracted from GIS analysis (Figure 2-12). The input hydrographs obtained to both ponds locations were considered as boundary conditions in a 2D hydraulic model developed in HEC-RAS for the Sobral da Adiça village.

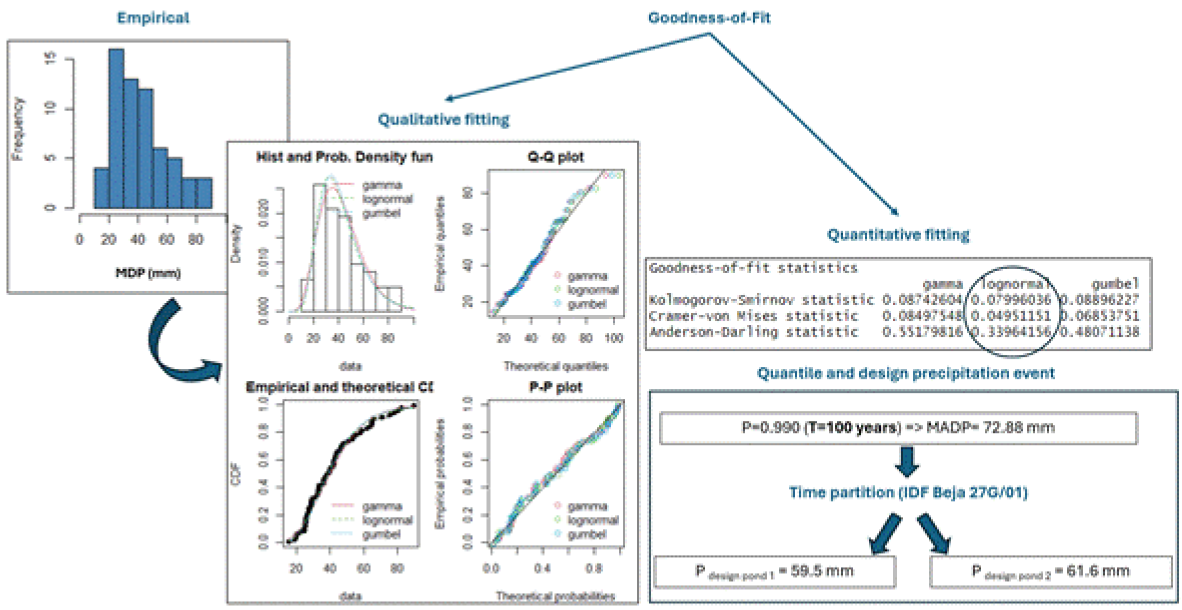

Figure 2-14 Maximum annual daily precipitation probability fitting and quantile estimation (P=0.99 | T=100 years).

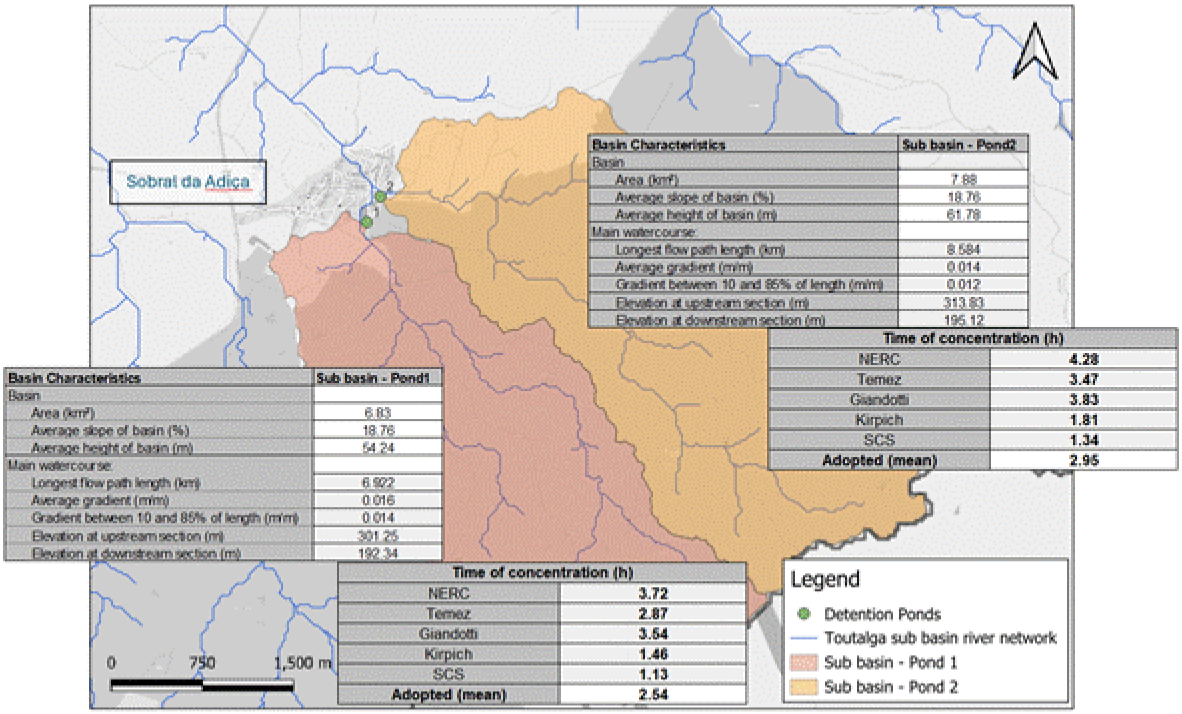

Figure 2-15 Ponds location upstream of Sobral da Adiça village and respective sub basin characteristics

The configuration of the hydraulic model consisted of the following:

Table 2-2 Hydraulic model setup (main characteristics).

Terrain data (most critical)	Geometry Setup (2D domain)	Hydraulic parameters	Boundary and Initial conditions
Sobral da Adiça urban area: 0.5 m coupled high resolution DSM and DEM	Multiple mesh sizes (refinement regions):	Manning's n values (spatially varied based on LULC COSc 2024, 10 m)	2 inflow hydrographs (upstream - pond 1, 2)
Urban drainage system geometrical correction: 0.1 m high resolution DEM (1D derived ensuring prismatic section)	- 2 m in Urban Drainage System	Curve number (spatially varied and based on GCN, AMCII, 250 m)	Normal depth (downstream)
Ponds sub basins: 0.5 m high resolution DEM	- 5 m in Sobral da Adiça (207276 cells) - 10 m ponds sub basins (178502 cells)	Infiltration layer (compute losses based on previous land use and curve number)	Start with dry conditions (no pre warming)
	-Breaklines positioning (to preserve the terrain features and refine computational points)		

The 0.5 m DEM required preprocessing and correction in the urban area in order to accurately capture the geometry of the urban drainage system using a 1D geometry editor; it was ultimately converted into a 0.1 m resolution. An on-site geometric survey was conducted, and 10-meter distances between cross-sections were used in the model to accurately represent the prismatic channel system (including 3 sections and 1 junction). To capture most urban structures with a good level of geometric detail, buildings were treated as blocks by combining the DSM with the DEM, both of which had the same resolution of 0.5 m (the DSM and DEM were acquired by the same LiDAR sensor on the same date).

2.4 Hydrological modelling / monitoring Maglavit/Danube River catchment

2.4.1 Site description and monitoring network

The Romanian Living Lab (LL-RO) is situated on a stretch of former Danube River floodplain between the villages of Salcia and Maglavit, in Dolj County, south-western Romania. The site encompasses a range of land uses including abandoned fish ponds, arable land, planted forest and managed pasture, representative of the degraded floodplain landscapes common across the middle Danube corridor. The hydrological regime is characterised by a strong seasonal water deficit: mean annual precipitation is approximately 554 mm while mean annual reference evapotranspiration (ET_0) exceeds 1073 mm, yielding a structural deficit of approximately −519 mm yr^{-1} (1991–2023 Calafat station record).

An automatic weather station was installed at the site in June 2025 and records air temperature, relative humidity, global solar radiation, wind speed at 2 m, and precipitation at 10-minute intervals. These data are used to compute daily ET_0 following the FAO-56 Penman-Monteith equation (Allen et al., 1998; Figure 2-16). Five soil moisture monitoring stations (sensors C-01 to C-05) were installed across the site, each measuring volumetric water content (VWC) at six depths: 10, 20, 30, 45, 60, and 90 cm, at hourly resolution (capacitance probes). The monitoring period analysed here covers June 2025 to January 2026.

The site is located in the Oltenia Plain, one of the driest and warmest sub-regions of Romania, characterised by a semi-arid continental climate with hot summers and mild winters. The broader Salcia–Maglavit corridor was historically part of the active Danube floodplain before river regulation works in the 1970s severed lateral connectivity. The resulting landscape, now isolated from regular flood pulses, is particularly vulnerable to soil moisture deficits during summer, as groundwater tables are too deep to sustain capillary rise into the root zone under current conditions. This makes the site representative of a large class of degraded floodplain sites across the lower and middle Danube where reconnection to river dynamics is being explored as a Nature-based Solution.

The monitoring network was designed to capture the full seasonal range of soil moisture dynamics, from summer desiccation to autumn and winter recharge. Sensor depths were selected to bracket the root zone (0–45 cm), the transition zone (60 cm), and the deeper vadose zone (90 cm), allowing the wetting front progression and drainage dynamics to be tracked continuously. The weather station data enable computation of the full Penman–Monteith ET_0 formulation (Figure 2-16), requiring all four measured input variables (air temperature, relative humidity, solar radiation, and wind speed), which distinguishes this monitoring setup from simpler installations that rely on temperature-only methods.

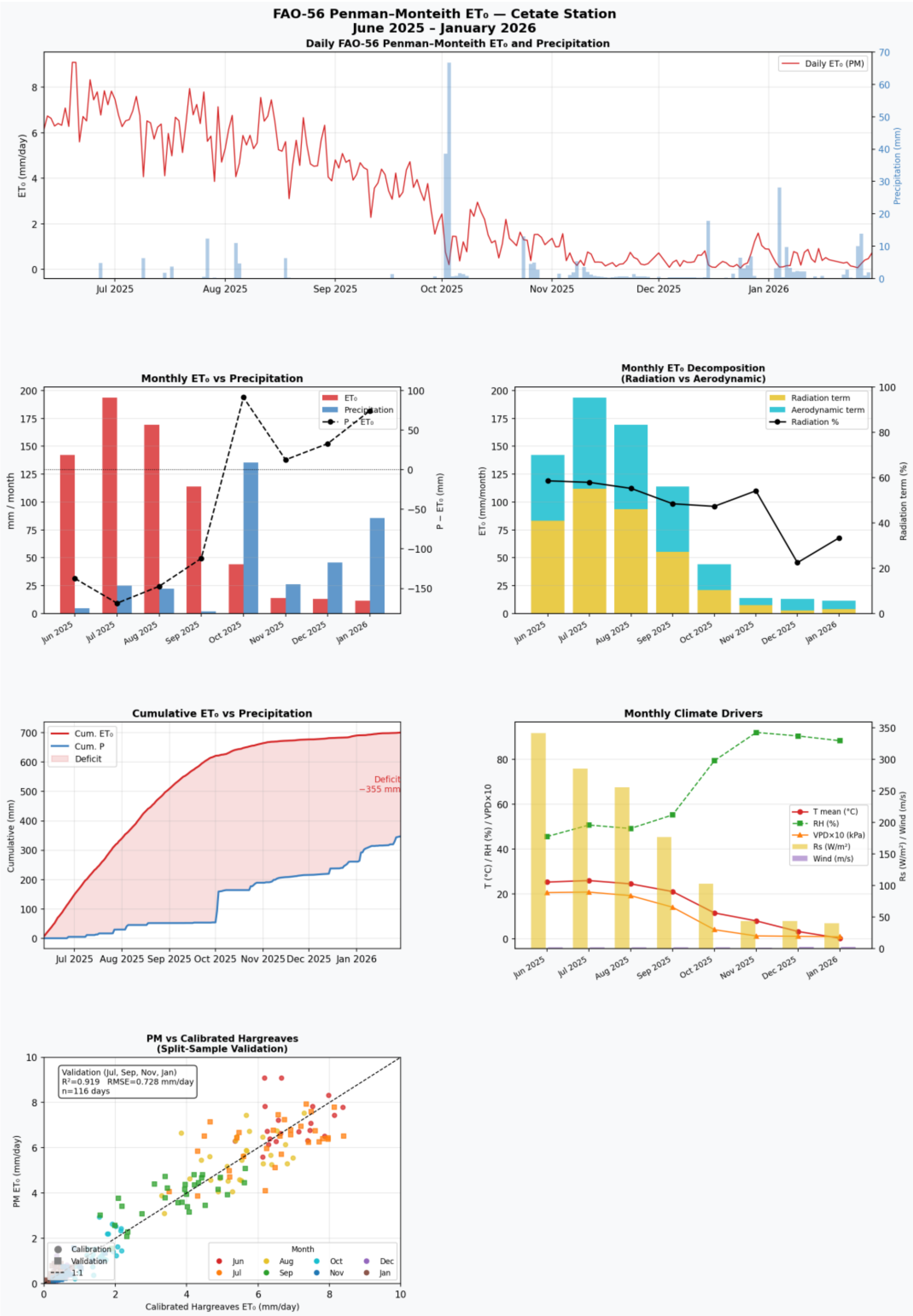

Figure 2-16 FAO-56 Penman-Monteith ET_o analysis, Cetate station (June 2025–January 2026). Top (full width): daily ET_o (red line) and precipitation (blue bars). Centre-left: monthly ET_o vs precipitation with cumulative P–ET_o deficit. Centre-right: monthly ET_o decomposition into radiative (yellow) and aerodynamic (teal) components with radiation fraction (%). Bottom-left: cumulative ET_o and precipitation with deficit shaded. Bottom-right: monthly climatic drivers (mean temperature, relative humidity, VPD, solar radiation, wind speed). Bottom row: Hargreaves-Samani vs FAO-56 PM ET_o calibration scatter (split-sample validation, R^2=0.919, RMSE=0.73 mm day^{-1}, n=116 days).

2.4.2 Historical climate data

A 33-year daily climate archive (1991–2023) from Calafat meteorological station (~12 km from the Living Lab) was used to characterise the long-term hydroclimatic context. Reference ET_0 for the historical period was estimated using the Hargreaves-Samani method, calibrated against FAO-56 PM ET_0 (slope = 0.420, intercept = −0.093, R^2 = 0.919, RMSE = 0.73 mm day^{-1}, n = 116 days). The SPEI-12 drought index (Vicente-Serrano et al., 2010) was computed to characterise drought variability. Figure 2-17 shows a warming trend of +0.62°C $decade^{-1}$ and increasing ET_0 demand of +40 mm $decade^{-1}$, consistent with the deepening structural deficit.

Analysis of the annual precipitation record reveals high inter-annual variability (range 259–979 mm yr^{-1}; min in 2000, max in 2014), confirming that the structural deficit is not simply a consequence of uniformly low rainfall but rather of extreme atmospheric demand combined with episodic rainfall failures. Of the 33 years on record, 8 experienced at least one month with SPEI-12 below −1.5 (severe drought classification), while 7 years recorded strongly positive SPEI-12 values exceeding +1.5 (notably wet conditions). The frequency and severity of drought episodes have increased after 2010 relative to the earlier part of the record, consistent with the regional warming trend.

The seasonal distribution of precipitation strongly reinforces the summer water deficit. Summer months (June–September) account for only approximately 35% of annual precipitation (mean ~195 mm), while contributing the majority of atmospheric demand: mean monthly ET_0 values reach 172 mm in June, 187 mm in July, and 166 mm in August. This mismatch between supply and demand is the primary driver of recurrent summer water stress at the site and across the broader Danube floodplain region. The Hargreaves-Samani calibration approach (Figure 2-16, bottom right) ensures that these historical ET_0 estimates are consistent with the FAO-56 Penman-Monteith standard, enabling direct comparison between the monitoring-period and long-term climate records.

The 33-year temperature record (Figure 2-17, bottom-left) shows a statistically highly significant warming trend of +0.62°C $decade^{-1}$ (R^2 = 0.485, $p < 0.001$), with mean annual temperature rising from 12.5°C in the 1991–2000 decade to 13.9°C in 2014–2023 — an increase of 1.4°C over approximately three decades. The warmest year on record was 2023 (14.7°C) and the coolest was 1991 (11.4°C). This warming trend drives a corresponding increase in atmospheric water demand: ET_0 has risen from approximately 942 mm yr^{-1} in 1991 to 1126 mm yr^{-1} in 2023, an increase of approximately 184 mm over the record, consistent with the linear trend of +40 mm $decade^{-1}$ ($p < 0.001$).

In contrast to the clear temperature and ET_0 trends, annual precipitation shows no statistically significant trend over the 33-year record (Figure 2-17, top; $p = 0.069$), with high inter-annual variability (coefficient of variation 25%, standard deviation 137 mm yr^{-1}). The driest years were 2000 (259 mm), 1992 (303 mm), and 2011 (333 mm), while the wettest were 2014 (979 mm), 2005 (810 mm), and 2016 (726 mm). Eight of the 33 years recorded an annual deficit exceeding −600 mm (1992, 1993, 1994, 2000, 2011, 2012, 2019, and 2022), confirming that severe drought years are not isolated events. Despite the absence of a significant precipitation trend, the structural deficit has widened because ET_0 continues to increase while precipitation remains stationary.

The SPEI-12 drought index (Figure 2-17, second row) reveals two multi-year drought episodes of particular severity in the record. The first, centered on 2000–2001, produced the most negative SPEI-12 value in the series (−2.24 in January 2001, corresponding to an extreme drought classification), driven by the exceptionally low precipitation of 2000 (259 mm) coinciding with high ET_0 demand. The second and longer episode ran continuously from October 2011 to March 2013, 17 consecutive months below SPEI-12 = −1.0, with a minimum of −1.76 in September 2012. In addition, a shorter but severe drought is visible in 2022 (SPEI-12 = −1.71), suggesting a recent re-intensification consistent with the warming trend. Wet anomalies are concentrated in 2014–2015 (SPEI-12 up to +3.05 in 2015, the highest value in the record) and 2005–2006, both corresponding to years of exceptionally high precipitation.

The SPI-12 (Figure 2-17, third row), which uses only precipitation (no ET_0), tracks the SPEI-12 closely, indicating that the main driver of drought variability at this site is precipitation deficit rather than ET_0 anomalies alone. Divergence between SPI and SPEI is most visible in recent years, where SPI shows neutral or slightly positive conditions in some years that SPEI classifies as near-drought, a direct consequence of rising ET_0 demand eroding even near-average rainfall years. This divergence is expected to increase under continued warming and represents the mechanism by which climate change gradually converts currently moderate precipitation years into effective drought years, without any change in the precipitation amount itself.

The annual water deficit panel (Figure 2-17, bottom-right) confirms these observations. The long-term mean deficit is −519 mm yr^{-1}, but individual years range from −32 mm in 2014, when great rainfall nearly matched demand, to −882 mm in 2000. The deficit shows no statistically significant trend ($p = 0.87$), consistent with the competing influences of increasing ET_0 (deepening deficit) and slightly increasing though non-significant precipitation. Decade-level means illustrate the interplay:

the 1991–2000 decade had the most negative mean deficit (−558 mm yr^{-1}) and the lowest mean precipitation (477 mm yr^{-1}); the 2001–2010 decade was the mildest (−456 mm yr^{-1}, mean P = 594 mm yr^{-1}); and the most recent period (2011–2023) shows an intermediate but worsening deficit (−537 mm yr^{-1}) at substantially higher temperatures (mean 13.7°C), indicating that the same precipitation now sustains a larger atmospheric demand and therefore delivers less net soil water recharge.

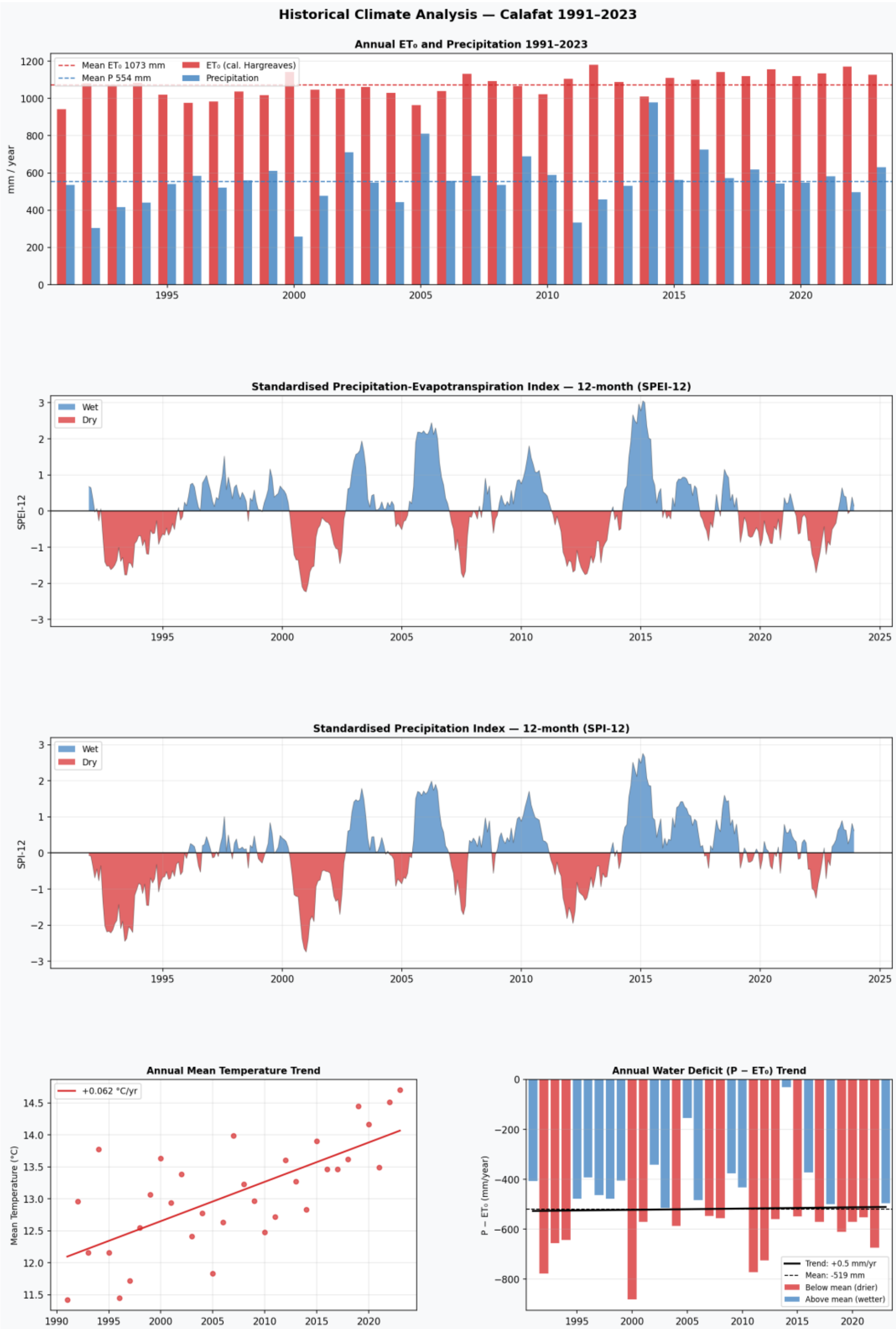

Figure 2-17 Long-term hydroclimatic analysis, Calafat station 1991–2023. Top (full width): annual ET_0 (Hargreaves, red) and precipitation (blue) with long-term means. Second row (full width): SPEI-12 drought index (blue = wet, red = drought). Third row (full width): SPI-12 standardised precipitation index. Bottom-left: annual mean temperature with linear trend (+0.62°C decade^{-1}). Bottom-right: annual water deficit (P − ET_0) with long-term mean (−519 mm yr^{-1}).

2.4.3 Soil moisture monitoring

The soil moisture heatmap (Figure 2-18) provides a continuous record of profile wetness at all six depths from June 2025 to January 2026. Three hydrological phases are visible: (1) progressive summer desiccation from June through September; (2) rapid recharge during the October 2–3 event (105 mm in 48 h), visible as a green front propagating downward; and (3) sustained wet conditions through November–January. Inter-sensor variability was low, confirming that the observed dynamics are spatially representative of the site.

Comparison of mean VWC between the summer drought period (June–September 2025) and the subsequent wet season (October 2025–January 2026) illustrates the magnitude of seasonal soil moisture cycling at this site. At 10 cm depth, mean VWC increased from 11.6% in summer to 18.1% in the wet season; at 20 cm from 7.5% to 20.0%; at 45 cm from 7.8% to 18.7%. The deepest sensor at 90 cm showed a similar seasonal amplitude (11.2% to 18.4%), indicating that the entire monitored profile experiences substantial seasonal wetting and drying cycles, not only the surface layers.

Inter-sensor variability at 45 cm depth was modest, with site-mean VWC ranging from 11.4% (sensor C-01) to 15.9% (sensor C-05) and standard deviations between 4.1% and 8.2%. This spatial variability likely reflects small differences in soil texture and bulk density across the 200-ha site. Despite this variability, all five sensors tracked the seasonal dynamics consistently, confirming that the site-averaged soil moisture signal is robust and that the single-layer model calibrated against the site mean is representative of the broader site hydrology.

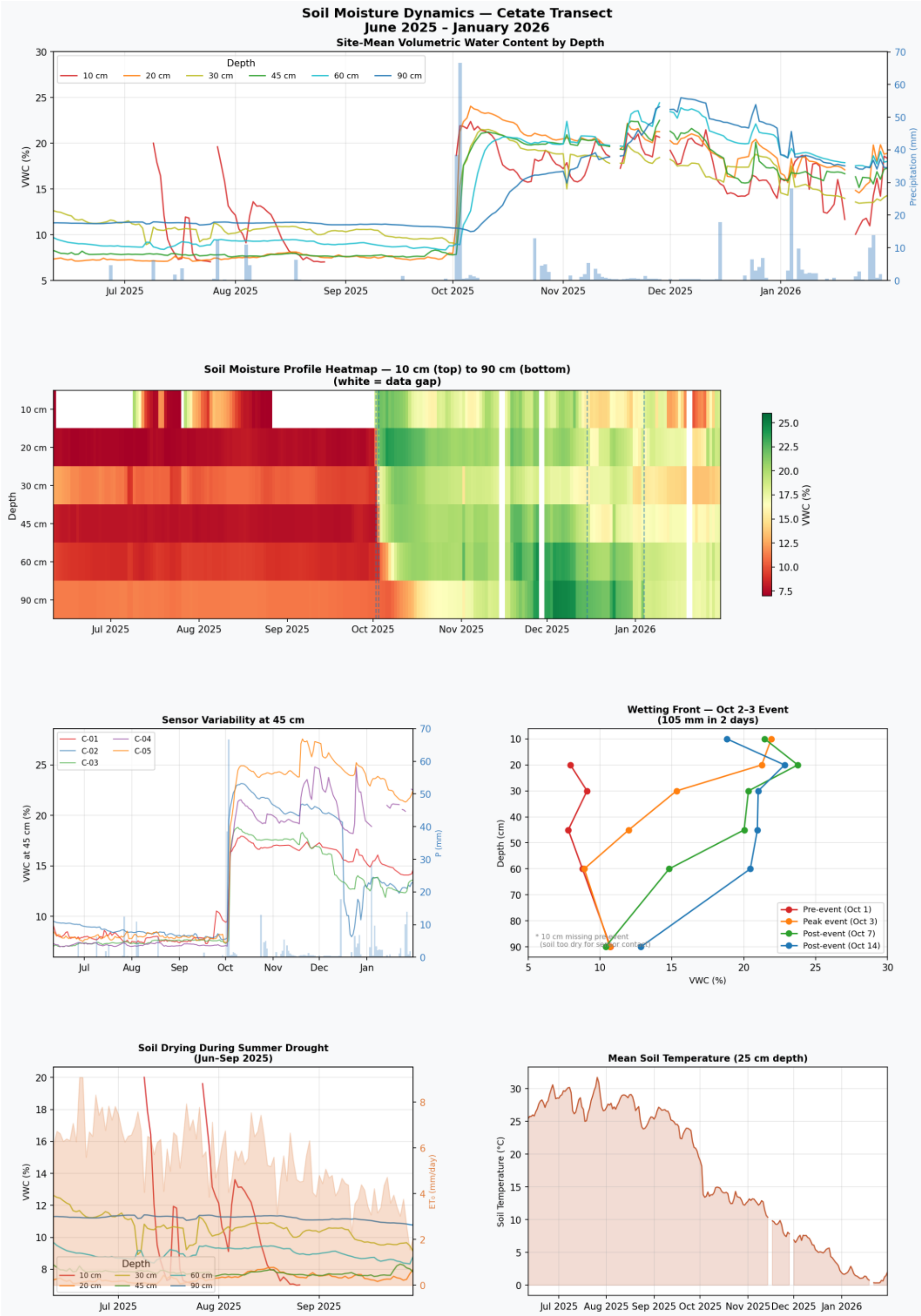

Figure 2-18 Soil moisture monitoring results (June 2025–January 2026). Top (full width): site-mean VWC time series at six depths (10–90 cm) with precipitation. Second row (full width): soil moisture profile heatmap (depth on y-axis, time on x-axis; red = dry, green = wet, white = data gap). Centre-left: VWC at 45 cm for all five individual sensors (C-01 to C-05) showing inter-sensor variability. Centre-right: wetting front depth profiles for the October 2–3 event at four dates (pre-event 1 Oct, peak 3 Oct, 7 Oct (day +5), 14 Oct (day +12)). Bottom-left: soil VWC drying progression by depth during summer drought (June–September 2025) with ET_o. Bottom-right: mean soil temperature at 25 cm depth.

2.4.4 Soil water balance model

A single-layer bucket-type soil water balance model was developed to simulate root zone SWS (mm) in the 0–45 cm profile. The model solves a daily water balance: SWS(t) = SWS(t−1) + Infiltration(t) − ETa(t) − Deep drainage(t). Infiltration is calculated from available rainfall plus a surface ponding store (Sp,max = 33.7 mm), subject to infiltration rate k_inf. Deep drainage is controlled by parameter k_p when SWS exceeds FC. Actual evapotranspiration ETa = Kc,max × ET_0 × s(SWS), where s(SWS) = [(SWS − WP)/(FC − WP)]^α, constrained to [0, 1].

Calibrated parameter values are: FC = 96.2 mm, WP = 35.3 mm, AWC = 60.9 mm, k_inf = 0.981, k_p = 0.717, Kc,max = 0.303, α = 0.300, Sp,max = 33.7 mm. The observational water balance for the monitoring period (Figure 2-19) illustrates the summer stress regime and the transition to wet-season recharge.

The monthly partitioning of the water balance highlights the extreme nature of the 2025 summer drought. Actual evapotranspiration in June, July, August, and September was only 14, 45, 39, and 6 mm respectively, compared to atmospheric demands of 142, 193, 169, and 114 mm. By September, the soil was so desiccated that ETa had effectively ceased (6 mm over 30 days = 0.2 mm day^{-1}), despite continuing atmospheric demand. In contrast, once the soil recharged in October, the model correctly captures the resumption of drainage-dominated dynamics: 19 days with drainage exceeding 1 mm were recorded between October and January, predominantly in the two weeks following the 105-mm event.

The shape parameter α = 0.300 in the water stress function produces a concave relationship between relative soil water content and transpiration reduction, consistent with the gradual stomatal response typical of drought-tolerant vegetation in semi-arid environments, where transpiration is maintained until soil water approaches the wilting point. Kc,max = 0.303 represents the maximum attainable crop coefficient under non-stressed conditions for the sparse, mixed vegetation cover of the site, and is substantially lower than values reported for dense crops or forests (typically 0.8–1.2), reflecting the open and degraded nature of the floodplain vegetation. The surface ponding store Sp,max = 33.7 mm accounts for the micro-topographic depressions present in the former fish pond landscape, which temporarily retain water before it infiltrates.

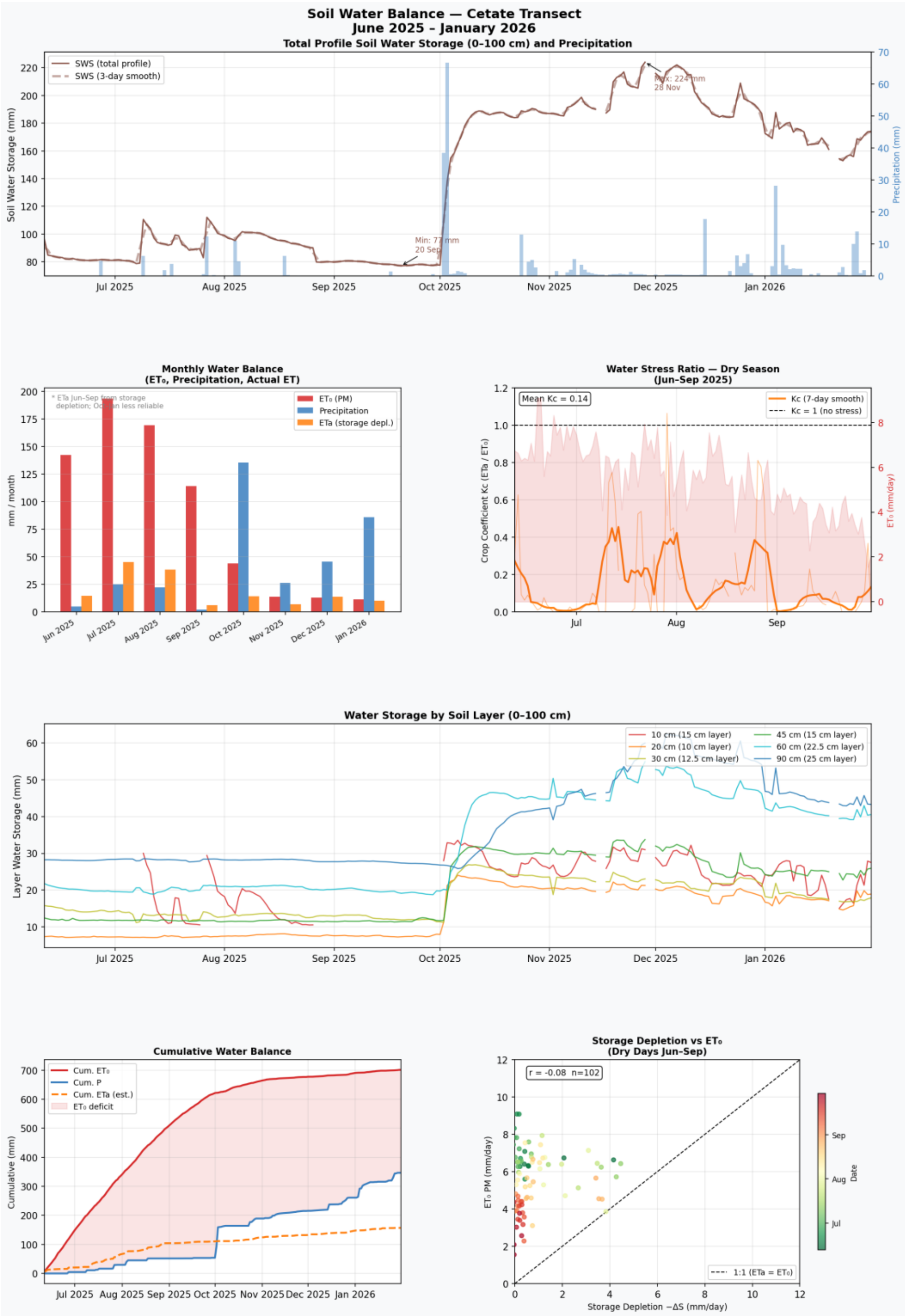

Figure 2-19 Observational soil water balance (June 2025–January 2026). Top (full width): total profile soil water storage (0–100 cm) with daily precipitation; minimum (77 mm, 20 Sep) and maximum (224 mm, 28 Nov) annotated. Centre-left: monthly water balance components (ET_0 demand, actual ETa, precipitation, ETa from storage depletion). Centre-right: crop coefficient Kc (ETa/ET_0) during the dry season (June–September 2025) with mean Kc = 0.14 indicated. Third row (full width): water storage by individual soil layer (0–100 cm, six layers). Bottom-left: cumulative water balance (ET_0 demand, modelled ETa, precipitation, drainage Q). Bottom-right: daily storage depletion vs ET_0 scatter during dry days (June–September 2025).

2.4.5 Long-term hindcast and climate scenario analysis

The calibrated model was applied to the 33-year Calafat record to reconstruct annual water stress days (days when SWS < WP + 0.30 × AWC). Future climate impacts were assessed using a delta-change approach based on EURO-CORDEX ensemble median projections (Jacob et al., 2014) for RCP4.5 and RCP8.5 at 2041–2070 and 2071–2100. NbS sensitivity was evaluated by incrementally increasing FC by 10–50 mm above the calibrated baseline, simulating the effect of enhanced water retention measures.

The stress threshold of WP + 0.30 × AWC = 53.5 mm corresponds to a relative available water content of 30%, below which transpiration is assumed to decline substantially. This threshold was selected based on the observed onset of soil water depletion in the 2025 summer data, where the observed ETa/ET_0 ratio (Kc) began declining sharply as SWS approached this level. The 33-year hindcast using this threshold yields a mean of 19.3 stress days yr^{-1}, with 52% of years recording no stress at all. The distribution is strongly right-skewed: 17 of the 33 years had zero stress days, 7 had 1–20 days, 4 had 21–50 days, and 5 exceeded 50 days, confirming that drought stress at this site is episodic rather than chronic, but when it occurs it can be severe.

Stress occurrence is concentrated in late summer, the monthly frequency of stress days across the 33-year record is near zero in June, rises to 3% in July, peaks at 19% in September (with August and October both at ~16%), and returns to near-zero by November. This confirms that the vulnerability window is approximately August–October, when soil water reserves accumulated in winter and spring have been exhausted by cumulative summer demand. The delta-change approach for climate scenarios applies uniform temperature increments (yielding ET_0 increases of +53, +86, and +151 mm yr^{-1} for the three future scenarios) and proportional precipitation scaling (−23, −46, and −74 mm yr^{-1} respectively), extending the stress window progressively earlier into summer and later into autumn.

3 Results

3.1 Description of results of hydrological modelling / monitoring analysis for Liesingbach river catchment

3.1.1 Results of calibration and validation

The model demonstrates very good performance during both calibration and validation periods, successfully capturing the diurnal water temperature patterns observed in the Liesingbach river, see Figure 3-1. Both calibration and validation simulations closely follow the weekly pattern of observed data throughout the modeling period.

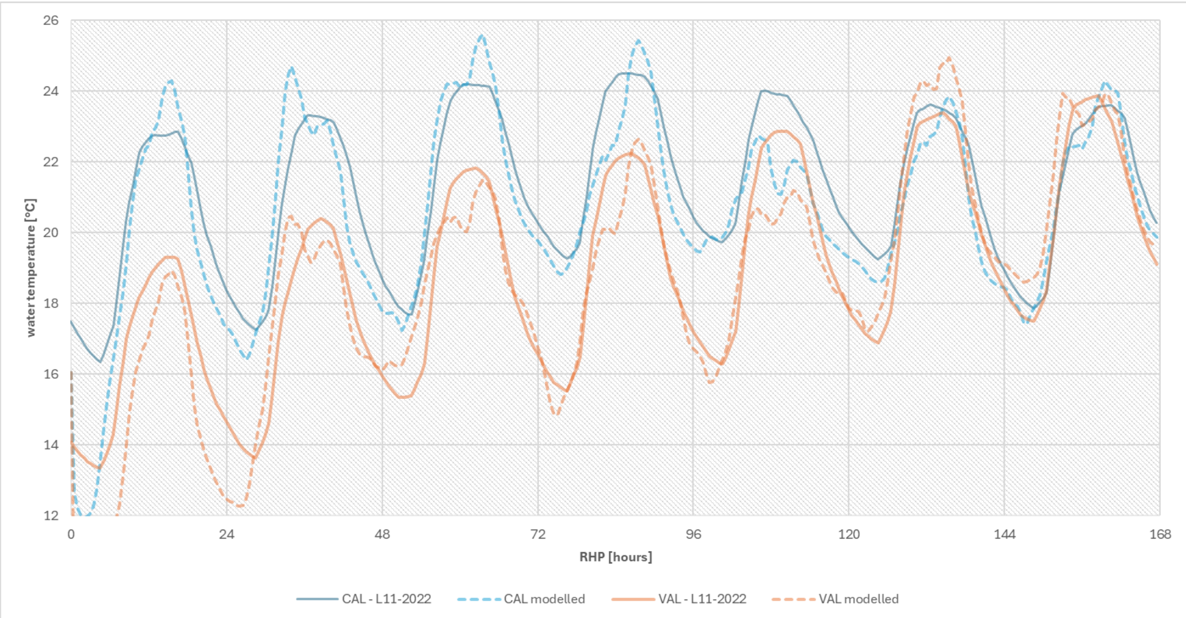

Figure 3-1 modelled and observed water temperature of the calibration (2022) and validation (2021) at the position of Logger 11

Based on the performance ratings (D. N. Moriasi *et al.*, 2007) the model achieves very good performance for both periods. The Nash-Sutcliffe Efficiency values of 0.75 (calibration) and 0.80 (validation) exceed the threshold of 0.75 for "very good" model performance. The near-identical NSE values between periods demonstrate excellent model transferability and robust parameterization. Additional performance parameter are listed in Table 3-1.

Table 3-1 Performance metrics (NSE, RMSE, MAE, PBIAS and r) for calibration and validation period

	NSE	RMSE	MAE	PBIAS	r
Calibration (2022)	**0.753**	**1.014**	**0.839**	**-2.1**	**0.914**
Validation (2021)	**0.807**	**1.156**	**0.918**	**-0.7**	**0.917**

3.1.2 Results of different vegetation densities under current and future climate

Following the calibration (2022) and validation (2021) phases, the model was applied to assess the influence of vegetation density on water temperature dynamics. The results of median historical river heat period demonstrate a clear relationship between vegetation density and water temperature patterns (Figure 3-2). All scenarios exhibit distinct thermal responses while maintaining the characteristic diurnal fluctuation pattern observed in the calibration and validation periods, with water temperatures ranging between approximately 17°C and 25°C and peak temperatures occurring during midday hours. Different situations of shading impact water temperature maxima by 4.9°C. A reduction of solar radiation transmissivity from the given vegetation to the p25 transmissivity scenario leads to a reduction of maximum water temperature of 3°C under current climate. Increasing vegetation to p50 transmissivity density contributes to 1.5° peak reduction in water temperature.

Regarding the current prevailing vegetation applied to a median climate change scenario (Figure 3-3), water temperatures during river heat periods in the years 2036-2065 are expected to rise by 2.2°. Reaching maximum values of 26.9°C. For the years 2071-2100 increases of 3.8° are predicted, leading to maxima of 28.5°C.

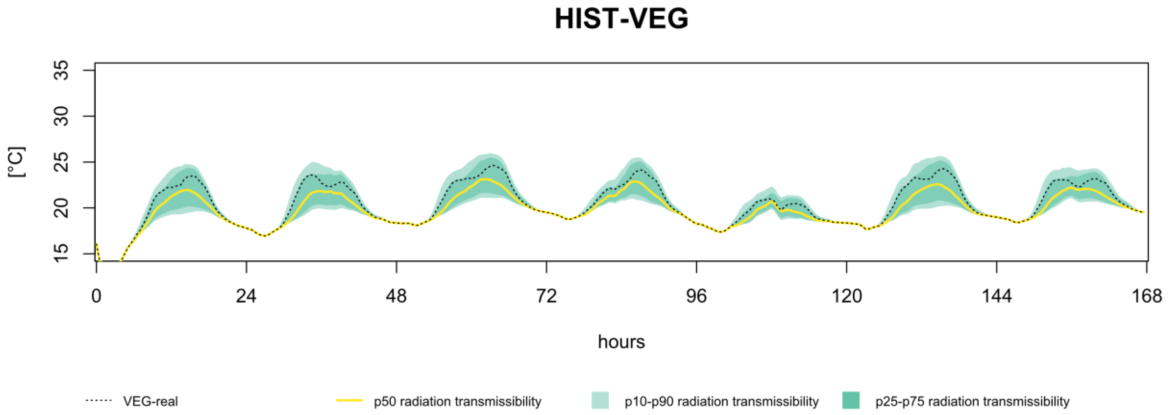

Figure 3-2 Results of the water temperature modelling with different scenarios: , , realistic vegetation with median meteorological data, and vegetation characteristic covering p10, p25, p50, p75 and p90 of calculated radiation input.

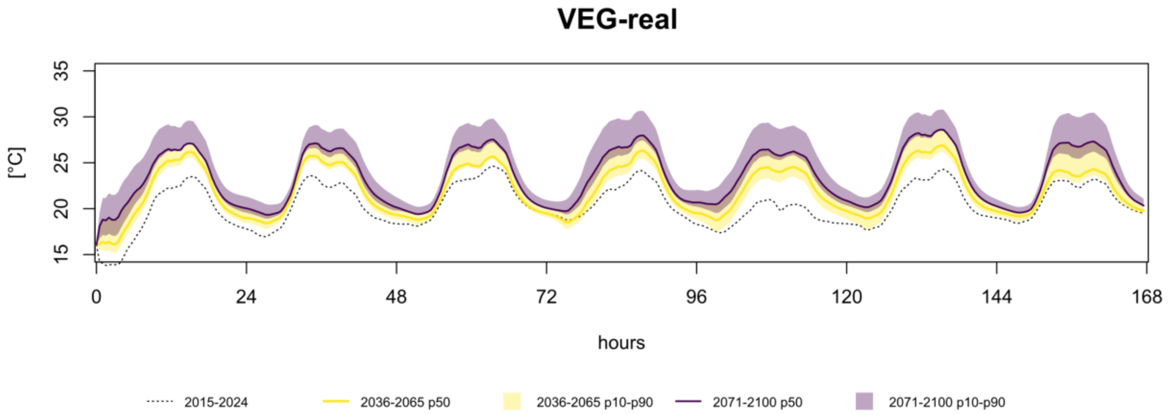

Figure 3-3 Results of the water temperature modelling with different vegetation scenarios for the median climate change projection.

3.2 Description of results of hydrological modelling / monitoring analysis for Vaerebro River catchment

3.2.1 Results of calibration and validation

The Værebro submodel is based on the latest DK-model (DK-model2026) and its calibrated parameters. Local calibration is not performed further but the submodel is evaluated based on the ability to represent reality, presented as differences between simulated and observed groundwater **heads**, stream **discharge** and stream **water levels**.

In the calibration of the parent model (DK-model2026, **three metrics for stream flow** are included; Kling-Gupta efficiency (KGE), water balance error (WBE), summer water balance (WBEs) and t**wo metrics** for groundwater levels; mean error (ME) and seasonal amplitudes. Four different categories for performance are used in the National model framework: Not sufficient, Screening, Approximate and Detail. These criteria are based on size and statistics of the discharge station, for more detail see Henriksen et al. (2022). Here we report the categories for the stations in Figure 3-4. The hydrographs at the four discharge stations, simulated as black and observed as blue can be seen in Figure 3-4.

Table 3-2 Discharge performance of the Værebro model

Q stations in Værebro model	KGE Type Q_{10}/Q_{90} eller Q_{50}	WBE Type Q_{50}	KGE	WBE
Q520022 *	1	2	**0.71**	**21%**
Q520034	1	1	**0.50**	**7%**
Q520037	1	1	**0.70**	**-21%**
Q520039 *	2	2	**0.67**	**-22%**
Q520040 **	2	3	**0.68**	**-26%**
Q520299 **	2	2	**0.81**	**-15%**

*stations included in DK-model calibration **observation period 2020 - 2024

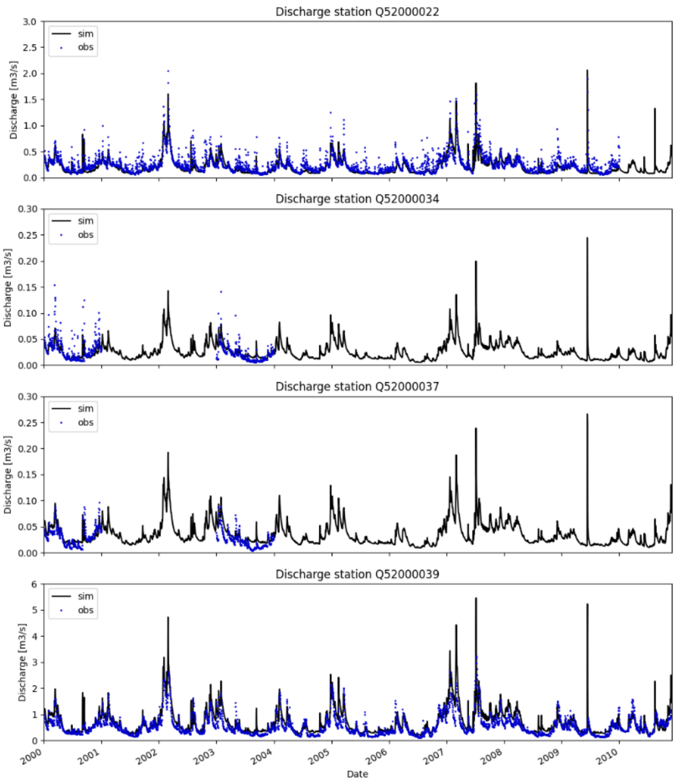

Figure 3-4 Hydrograph of the four discharge stations for the calibration period 2000-2010.

The performance criteria for the 6 stations are presented in Table 3-2 for WBE and KGE. The Vaerebro submodel performs at an acceptable level when using the criteria set up for the national scale, and the model can simulate stream discharge KGE for all stations except one at an approximate level.

To quantify the submodel' s ability to simulate groundwater heads, the mean error (ME) is used, and the distribution is shown in Figure 3-5. Overall groundwater head ME is for the entire submodel -1.2m, and MAE_{90} is 1.78, corresponding to a model that performs on the screening level.

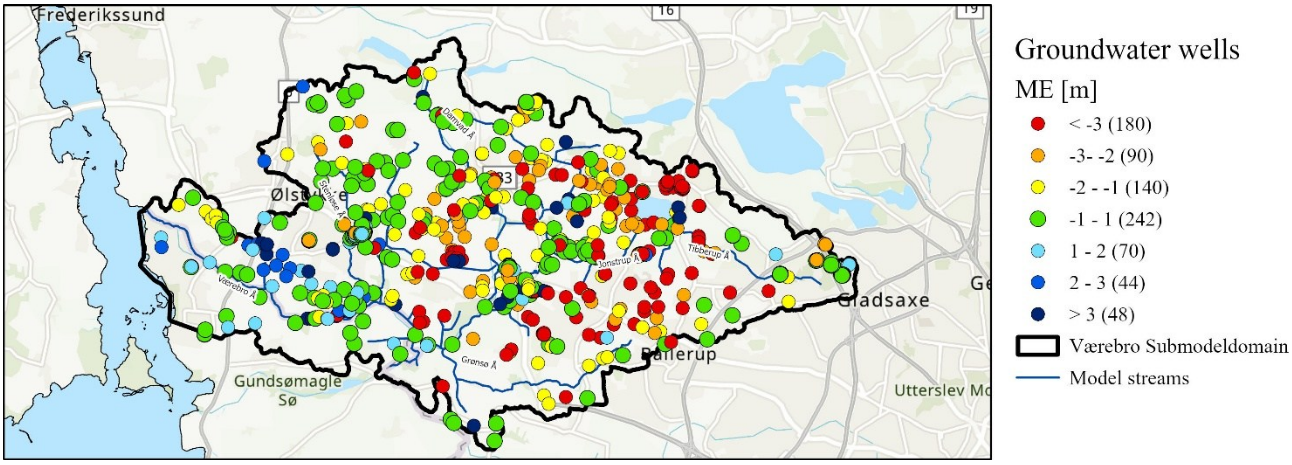

Figure 3-5 Location of groundwater level monitoring intakes in Værebro submodel and performance statistics for mean error (ME) in meters. Positive values show where the model simulates higher groundwater heads than observed.

3.2.2 Results of the modelled current hydrological setting

The Submodel results are presented for the entire simulation period of 1991-2024. The model serves as a basis for describing the general characteristics of the catchment and the spatial difference within it, as well as serving as the baseline to evaluate the impact of slow hydrology scenarios.

We focus on the water balance within the catchment, the discharge characteristics and extremes, and the spatial groundwater level distribution. For the water balance in the catchment, we analyse 11 subcatchments identified by a blue spot analysis of Strahler streamlines. The subcatchment 1-11 can be seen in Figure 3-6.

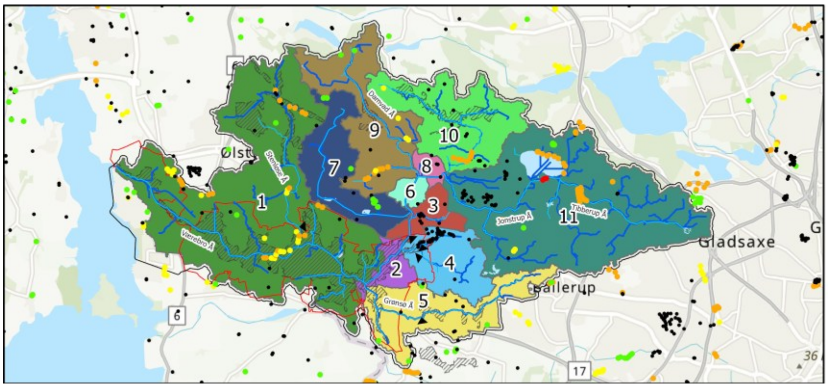

Figure 3-6 Map of the catchment with color representing the 11 subcatchments used for the water balance evaluation. Dots represent abstraction wells.

The overall water balance values for the entire basin can be seen in Figure 3-7. The highest evaporation occurs during summer, when the temperature is high, while the discharge is largest in winter, and more than double the amount than in summer. Drainage, especially tile drainage, constitutes a larger part of the discharge. And the groundwater abstraction is 13 % of the annual precipitation, the abstraction well locations can be seen in Figure 3-6.

Table 3-3 Overall water balance numbers of the Værebro catchment for the period of 1991-2024.

Variable	**Annual – mm/yr**
Precipitation	767
Actual evapotranspiration	530
Discharge at the outlet	161
Drainage	81
Abstraction	102

The water balance distribution for the 11 subcatchments can be seen in Figure 3-7. The evaporation is generally a larger part of the water balance in the upstream basins (8-11), while the baseflow components are large in the central basins and downstream basins.

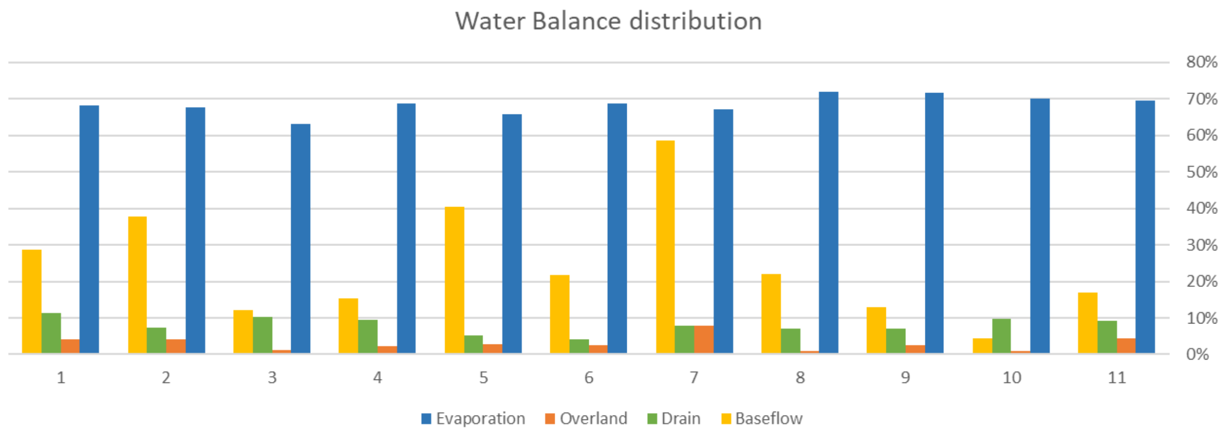

Figure 3-7 Distribution of water balance components for the 11 subcatchments.

The groundwater levels as predicted by the submodel can be seen in Figure 3-8. The mean depth of the groundwater table in the entire catchment is -3.7s meters below the surface. As can be seen from the figure, this covers a high degree of variability with areas of deeper groundwater levels in scattered sections across the catchment, especially in the center and north. The groundwater level is terrain-near levels in the river valleys, especially in the south, where a larger flat drained wetland area dominates. For the catchment, Q5 reaches -6.4 meters under the surface, with Q95 and Q99 reaching -1.9 and -1.5 meters, respectively.

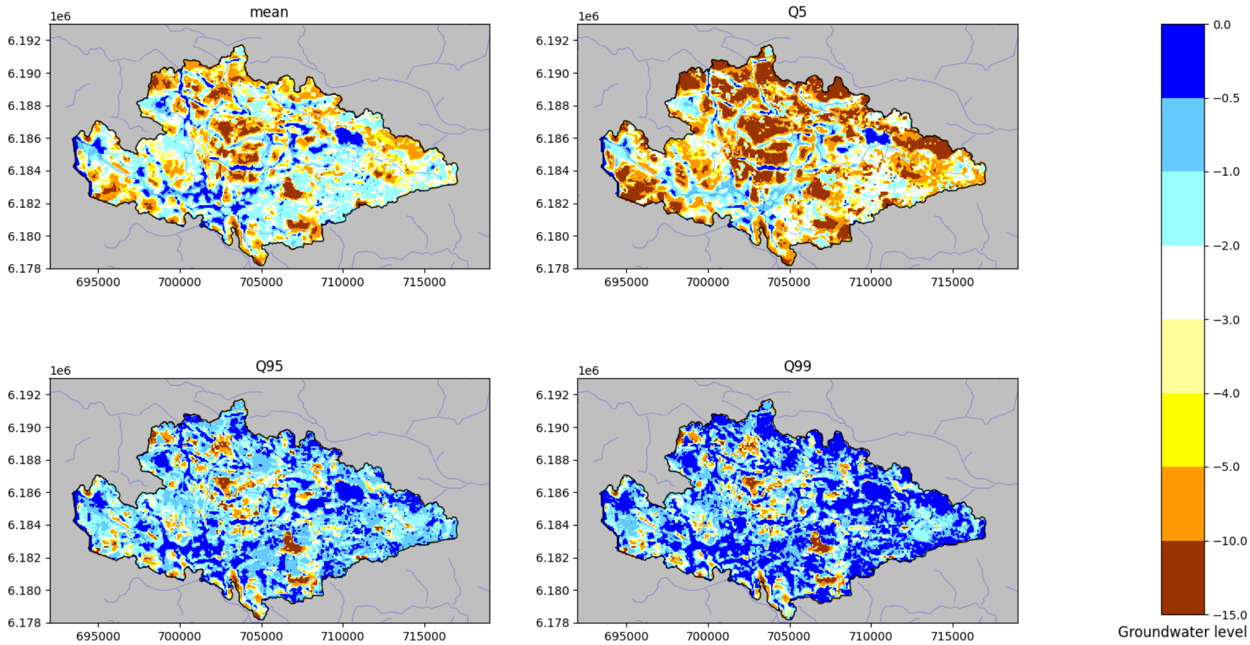

Figure 3-8 Groundwater levels as predicted by the baseline model for the period of 1991-2024. The four panels illustrate the mean groundwater, the 5th percentile, meaning the 5% driest timesteps (Q5), the 95th, and 99th percentile, meaning the 5% and 1% wettest, respectively, across the entire time series.

The spatial variation can also be illustrated in the boxplots in Figure 3-9. Here, it is clear that the largest special variability is during the dryest parts of the time series (Q5), across both seasons. While the special variability decreases during the wettest part of the period (Q99).

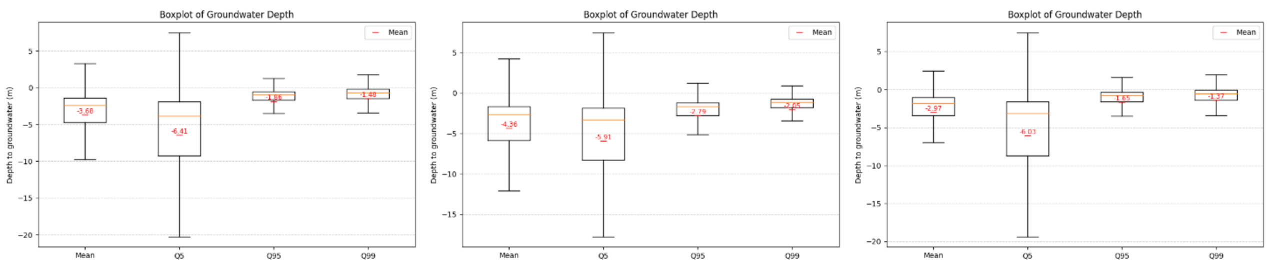

Figure 3-9 Boxplot of groundwater levels for the entire year (left) and time period, and divided into the summer (centre) and winter period (right)

3.2.3 Results of slow hydrology and anthropogenic scenarios

The anthropogenic and slow hydrology scenarios were then run through the hydrological model for the entire modelling period of roughly 30 years. As of now, we evaluate the impact of these scenarios by 10 indicators representing critical seasons and variables in relation to drought (#1-5) and flooding (#6-10) in the catchment.

The resulting impact can be seen in Table 3-4. In the table, blue indicates more water in the stream/groundwater compared to the current conditions, while orange indicates less water in the stream during winter. The discharge is the downstream flow in the watercourse/stream. Drought indicators for discharge are based on percentage changes in the annual and summer low flow, as well as the summer median discharge in the stream; while the flooding indicators for discharge are based on the high discharge in the stream annually and during winter, as well as the winter high flow. Blue means more water in the stream, and vice versa for orange.

The groundwater indicators are based on the depth to the groundwater table across the entire catchment. The impact is measured in cm change, with great depths (drier) being negative values (orange), and conversely, blue means the groundwater table is closer to the ground surface.

As seen in the table, mitigating drought conditions in the stream is only attached in the abstraction -50% scenario. All other scenarios lead to more dry conditions for discharge. Halfing the abstraction, however, has only limited effect on the dry conditions in the groundwater, whereas the removal of drain greatly enhances the groundwater levels in the indicators. This is related to an overall higher groundwater levels when the catchment is not artificially drained. For flooding, removing the drain and increasing the abstraction (+100%), mitigate the flooding indicators for discharge, while the groundwater level is still increased for the no drain scenaio. Overall, no scenario solves both issues, and the anthropogenic scenarioes generally have high impacts on the indicators.

Table 3-4 Overview of indicators for calculation under each of the scenarios. White= no to minimal effect; lightorange=small effect; orange= large effect; darkorange=very large negative effect; light blue=small positive effect; blue=large positive effect; darkblue= very large effect

	Hydrological variable	Indicator		Slow Hydrology Scenarios		Anthropogenic scenarios		
		Description	#	Afforestation	No drainage	Waste water scenario	Abstraction: -50%	Abstraction: +100%
Drought	Discharge [%]	Summer (Q50)	1	-1	-4	-22	13	-22
		Summer (Q5)	2	-9	-20	-144	87	-149
		Annual (Q5)	3	-4	-11	-56	34	-55
	Groundwater level [cm]	Summer (Q5)	4	-0.01	0.28	0	0.03	-0.06
		Annual (Q5)	5	-0.01	0.31	0	0.04	-0.07
FLooding	Discharge [%]	Winter (Q50)	6	-1	-25	-9	9	-14
		Winter (Q95)	7	0	-5	-3	6	-9
		Annual (Q95)	8	-1	-17	-5	7	-11
	Groundwater level [cm]	Winter (Q95)	9	-0.01	0.33	0	0.04	-0.08
		Annual (Q95)	10	-0.01	0.3	0	0.04	-0.07

The impacts reported here are, however, not constant across the entire catchment, as illustrated by the changes in groundwater levels between the historical reference and the no-drain scenario in Figure 3-10.

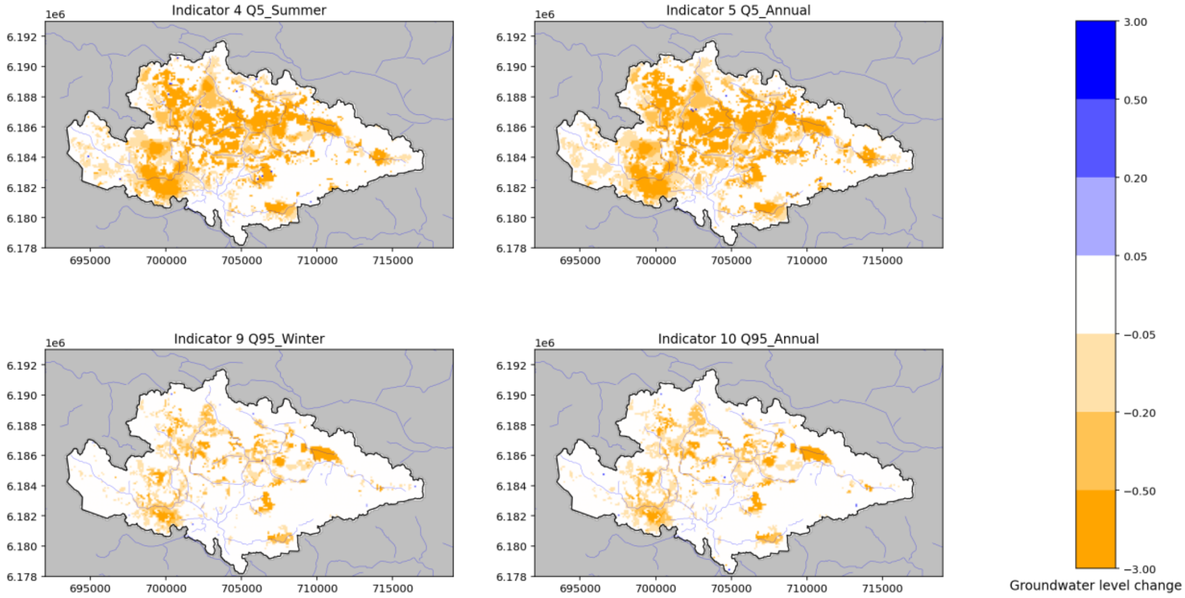

Figure 3-10 Spatial changes of groundwater level depth when comparing the reference situation to the +100% abstraction sceanrio for the four groundwater indicators.

3.3 Description of results of hydrological modelling / monitoring analysis for Toutalga River catchment

3.3.1 Calibration and validation of the monitoring–modeling demonstrator

For calibration, the event-based hydrological model used a flood event that occurred between January 20, 2025, and January 25, 2025, and for validation, an event that occurred between March 1, 2025, and March 13, 2025 (Figure 3-11).

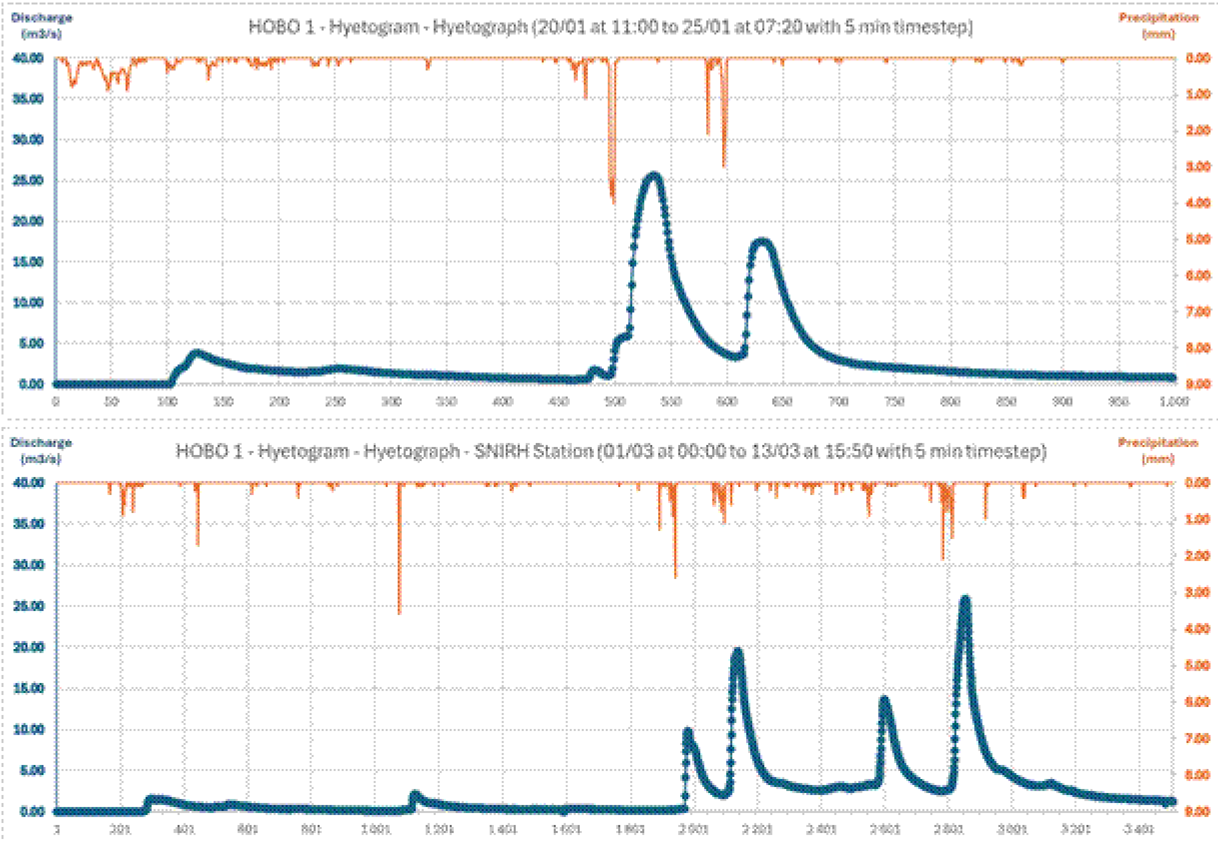

Figure 3-11 Hydrograph and Precipitation of the HOBO1 discharge station - calibration and validation events.

The optimization routine considered was the Peak-Weighted Variable Power with Max Iterations of 3000 and a Tolerance of 0.01 for convergence.

Peak-Weighted Variable Power	$Z = \sum_{i=1}^{N} \lvert q_s(i) - q_o(i) \rvert^{\frac{q_o(i)-q_o(min)}{q_o(peak)-q_o(min)}+1}$

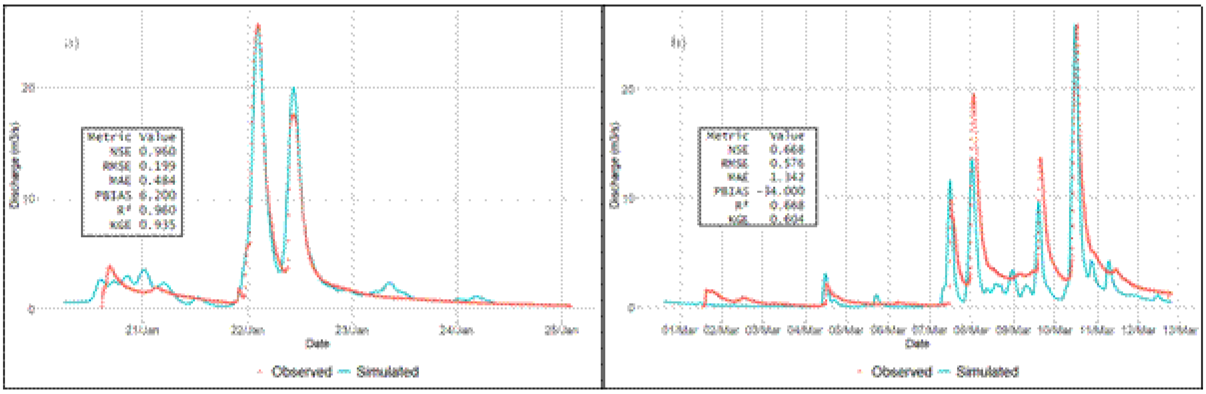

Figure 3-12 Simulated and observed discharge for the calibration (a) and validation (b) events in HOBO1 discharge station.

The model was able to capture the overall flow dynamics and the timing of successive peak discharges (Figure 3-12). The results highlight the value of integrating field monitoring, GIS analysis, and hydrological modelling to improve understanding of catchment behaviour under extreme conditions. This developed framework provided a robust foundation for subsequent hydraulic modelling, aimed at flood mitigation and climate adaptation for the Toutalga.

The model calibration achieved a **very good** performance while the validation just a **satisfactory** according to the final performance evaluation criteria considered (Moriasi *et al.*, 2015).

3.3.2 Pond design and hydraulic simulation results

The output hydrographs obtained from the HEC-HMS model resulted in a maximum flood peak of 16.1 m^3/s and 14.6 m^3/s and a flood volume of 118 080 m^3 and 88 725 m^3 for pond 1 and 2, respectively (Figure 3-13).

As previously mentioned, the overall objectives of the retention ponds are to control excess flood flows, support ecosystem integration, limit the maximum outflow in accordance with the hydraulic capacity of the main channel, and reduce flow velocities in the urban drainage system.

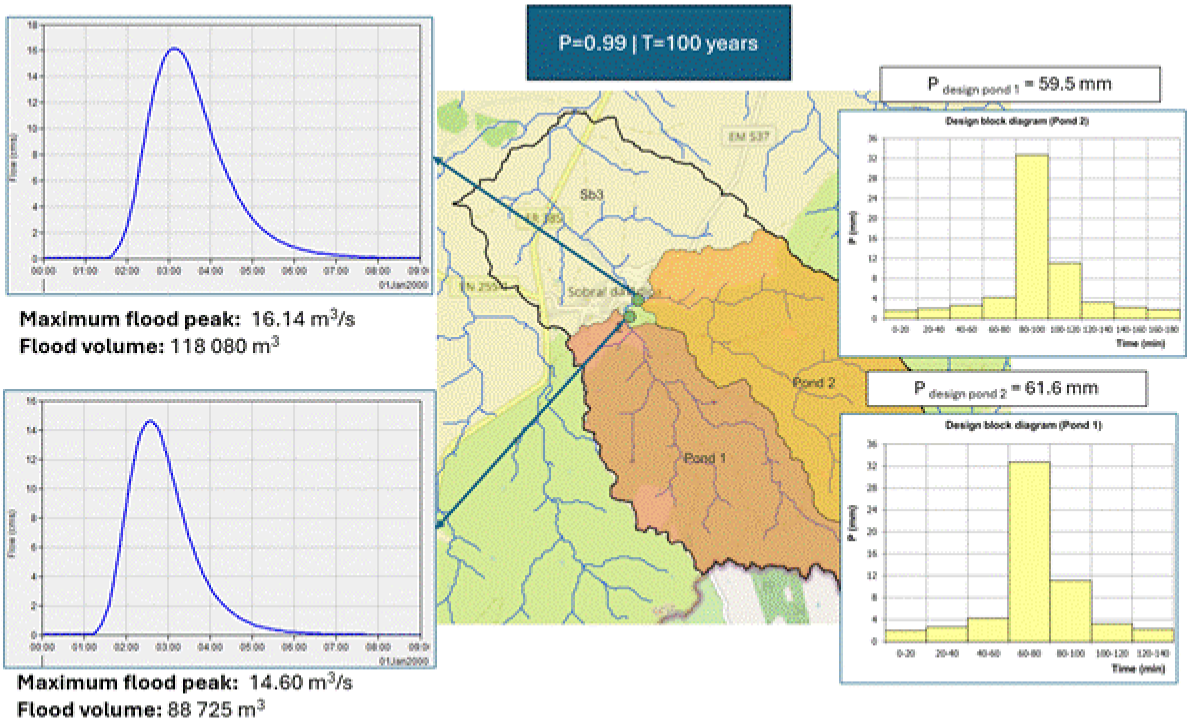

Figure 3-13 HEC-HMS model. Precipitation design hyetograph and model hydrograph outputs (T= 100 years).

Based on the field survey, the geometry, hydraulic characteristics, and flow capacity (Manning's formula) of the main channel system were evaluated, yielding a total capacity of 31 m^3/s (Figure 313).

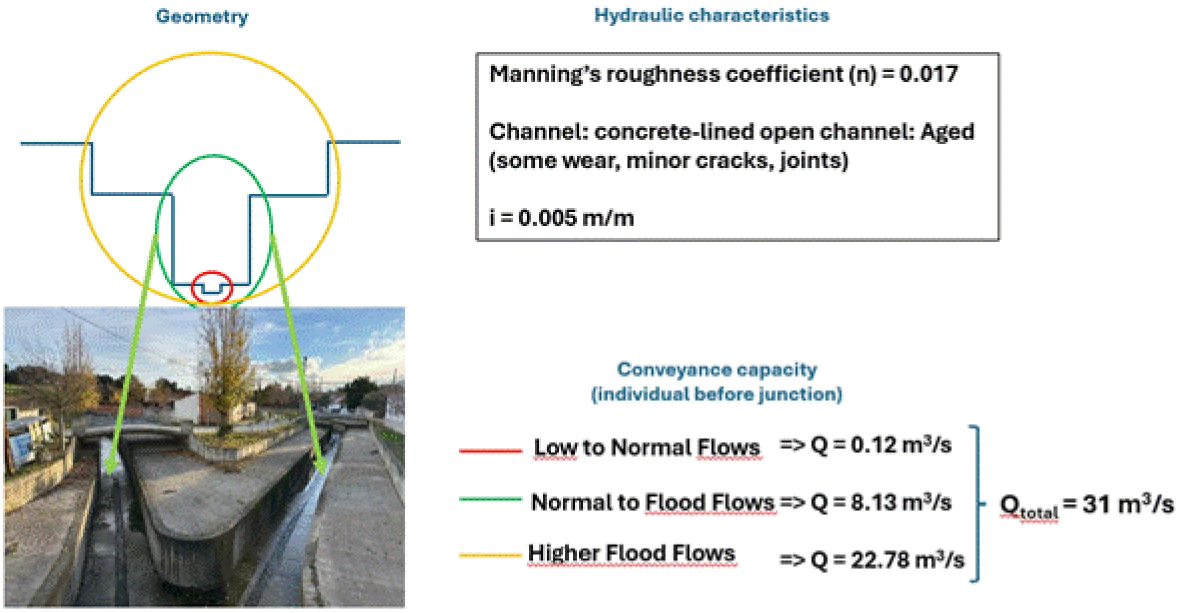

Figure 3-14 Actual Main Drainage System Conveyance Capacity from field survey (individual channel before the junction).

Regarding the ponds design a restricted maximum outflow of 4 m^3/s corresponding to half of the main individual channel conveyance capacity, was adopted as a first criteria to be considered as the maximum outflow capacity of both ponds 1 and 2 to be projected. This will allow for later channel geometry modification by including NBS solutions. Thus, the simulation of the pond's storage capacity was performed at 5-minute time step (TS), using the results of the HEC-HMS hydrograph as an input data and a fixed maximum discharge value as outflow, which resulted in a maximum required storage capacity of 45 500 m^3 and 64 900 m^3 for Pond 1 and Pond 2, respectively (Figure 3-15).

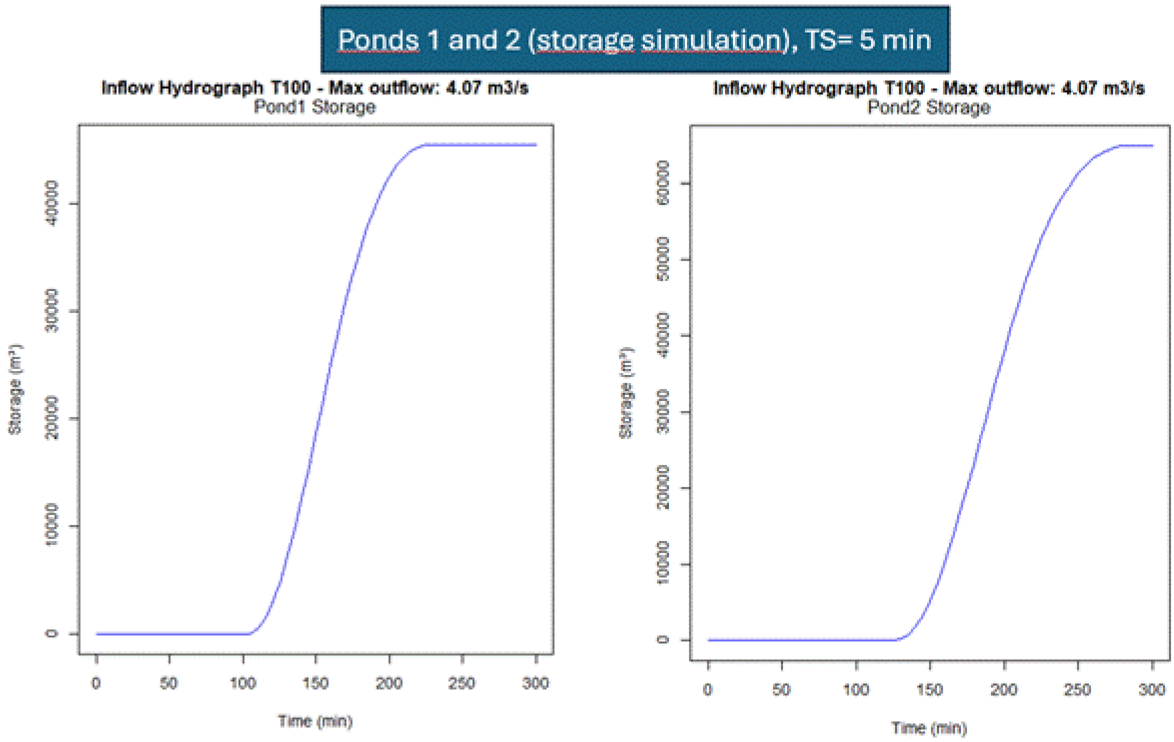

Figure 3-15 Storage capacity simulation for pond 1 and 2. HEC-HHMS hydrographs as inflow and a fixed outflow value at a 5 min time step.

The implementation of a 2D hydraulic model aimed to simulate the storage dynamics of the detention basins in response to a reference precipitation event (100-year), using a grid-based approach that took into account all the geomorphological aspects of each of the ponds sub-basins. Two scenarios were conducted: a) a 100 years flood event with the actual urban drainage system and; b) a 100 years flood event with the implementation of the ponds. The precipitation hyetograph considered alternate blocks, non-steady regime and the diffusion-wave equations for computing flow.

The terrain is the most critical aspect of a 2D model and so the geometric details were corrected in a 1D approach and integrated on the actual DEM mesh with a finer resolution (Figure 3-16).

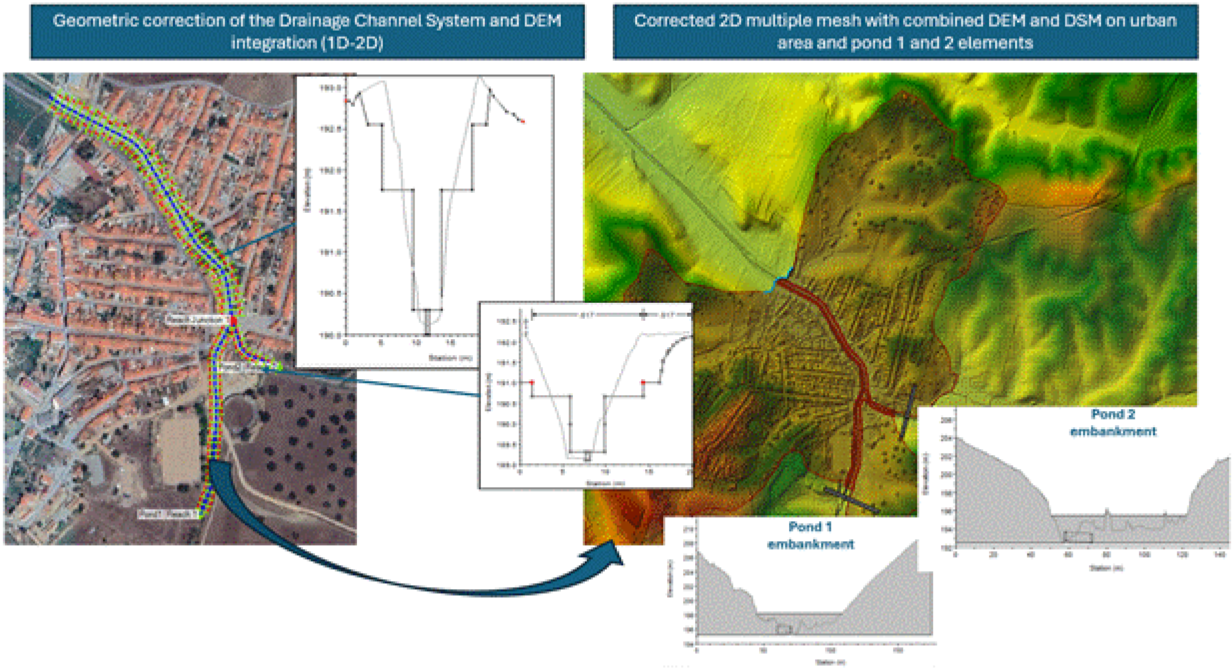

Figure 3-16 Urban drainage system geometry correction and DEM and DSM integration in urban area and ponds embankments.

The first results of Scenario 1 revealed that the flood was conveyed solely by the main drainage system (occupying most of the cross-section with the highest flow rate), with surrounding areas being flooded to a maximum depth of 1.5 m; overall, this seems to confirm that the system's actual capacity is insufficient to drain a 100-year flood. In scenario 2 by considering two embankments with 4 m high with one aligned culvert on each, with a diameter of 1 m, to ensure the maximum outflow, has resulted on a sufficient flowing capacity of the system, with the flow being conveyed only in the main channel. Future work is to prioritize NBS solutions as part of the main channel lining and to eliminate the high flood cross section to a better urban integration by reducing visual concrete impacts on urban environment.

3.4 Description of results of hydrological modelling / monitoring analysis for Maglavit / Danube River catchment

3.4.1 ET_0, precipitation and water balance (June 2025 – January 2026)

Over the monitoring period (11 June 2025 to 30 January 2026, n = 227 days), cumulative FAO-56 PM ET_0 reached 701 mm against total precipitation of 347 mm, yielding a water deficit of 355 mm. The summer months (June–September) were especially severe: ET_0 totalled 619 mm against only 54 mm of precipitation (deficit 565 mm), with peak daily ET_0 of 9.1 mm day^{-1} on 19 June 2025. This summer ET_0 total alone exceeds the mean annual precipitation for the region (554 mm). The contrast between atmospheric demand and rainfall supply is directly visible in Figure 213 (Hydrological modelling / monitoring Maglavit/Danube River catchment). Following the dry summer, the autumn period (October–January) delivered 293 mm of precipitation against only 82 mm of ET_0, producing a surplus of 211 mm that recharged the soil profile.

3.4.2 Soil moisture dynamics

Soil water storage in the 0–100 cm profile (full monitored depth) declined progressively through summer 2025, reaching a minimum of 77 mm on 20 September 2025 (mean profile VWC ~8.9%). All depths approached minimum recorded values (7.0–8.0% VWC) by late summer. The root zone (0–45 cm) SWS dropped to approximately 31 mm in late September, well below the calibrated wilting point (WP = 35 mm), indicating severe plant water stress throughout the late summer period.

The first significant autumn rainfall event on 2–3 October 2025 (105 mm in 48 h) triggered rapid recharge. Root zone SWS rose from 31 mm to 91 mm within one day and exceeded field capacity, reaching 103 mm, within two days. Maximum profile-integrated storage of 224 mm was recorded on 28 November 2025. Profile moisture remained near or above field capacity through December and January.

3.4.2.1 Wetting front dynamics and recharge controls

Analysis of 17 discrete rainfall events revealed a strong seasonal dependence of recharge depth (Figure 3-17). During summer (n = 6 events), no event produced a detectable VWC response below 30 cm depth. In contrast, 10 of 11 wet-season events produced a measurable response at 45 cm or deeper.

For the October 2–3 event (105 mm, 48 h): the 0–60 cm profile showed clear recharge within 2 days, while 90 cm responded on day +10. Spearman rank correlation identified antecedent cumulative ET_0 as the strongest control on maximum wetting front depth ($r = -0.740$, $p = 0.001$), with event rainfall as a secondary control ($r = +0.549$, $p = 0.022$).

Figure 3-17 Rec threshold analysis for 17 rainfall events (June 2025–January 2026). Top (full width): VWC time series at all six depths with individual event rainfall totals annotated; summer events (barely penetrating) vs wet-season events (deep recharge) visible. Centre-left: maximum recharge depth vs antecedent 7-day mean ET_0 (Spearman r = −0.740, p = 0.001; summer = red, wet season = blue). Centre-right: mean ΔVWC per event comparing matched event sizes (6–15 mm) between summer and wet season, showing identical rainfall produces very different responses. Bottom-left: wetting front depth profiles for the October 2–3 event (5 dates: pre-event, peak, day +3, day +6, day +12). Bottom-right: Spearman correlation with maximum recharge depth for three predictors (event size, antecedent SWS, antecedent ET_0). Bottom (full width): antecedent soil water storage vs maximum recharge depth bubble scatter (marker size = event rainfall; colour = antecedent ET_0).

3.4.3 Soil water balance model calibration and validation

The calibrated model reproduced observed root zone SWS (0–45 cm) with overall NSE = 0.916, RMSE = 8.7 mm, and PBIAS = 0.3% across the full monitoring period. Performance statistics for calibration and validation sub-periods are in Table 3-5 and Figure 3-18. The lower validation NSE (0.269) reflects the dynamic wet-season recharge–drainage cycle, which is more challenging for the single-layer structure. The model captures the seasonal trajectory and key stress dynamics with sufficient accuracy for the 33-year hindcast.

Table 3-5 *Model performance metrics (NSE, RMSE, PBIAS) for calibration and validation periods.*

Period	NSE	RMSE (mm)	PBIAS (%)
Calibration (Jun–Sep 2025)	0.531	5.9	0.6
Validation (Oct 2025–Jan 2026)	0.269	10.7	0.1
Overall (Jun 2025–Jan 2026)	0.916	8.7	0.3

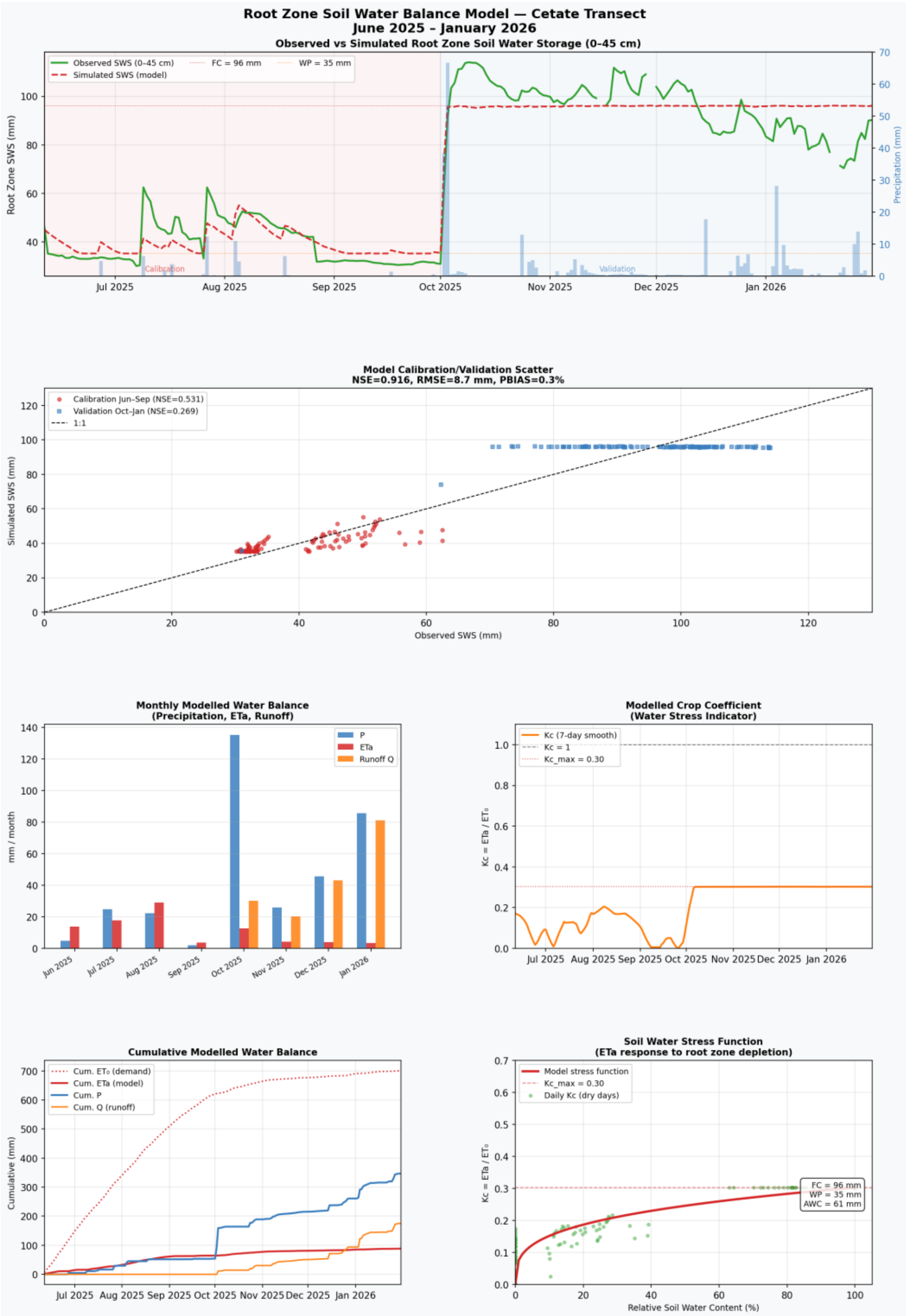

Figure 3-18 Soil water balance model calibration and validation. Top (full width): observed (green solid) vs simulated (red dashed) root zone SWS (0–45 cm) with precipitation; calibration (Jun–Sep 2025) and validation (Oct 2025–Jan 2026) periods shaded. Second row (full width): combined calibration/validation scatter plot of observed vs simulated SWS (overall NSE = 0.916, RMSE = 8.7 mm, PBIAS = 0.3%). Centre-left: monthly modelled water balance (precipitation, actual ETa, runoff Q). Centre-right: modelled crop coefficient Kc (ETa/ET$_0$) time series with Kc,max = 0.30 reference line. Bottom-left: cumulative modelled water balance (ET$_0$ demand, ETa, precipitation, Q). Bottom-right: soil water stress function showing /ET$_0$ vs relative soil water content (model curve vs observed daily Kc on dry days).

3.4.4 Long-term water stress analysis (1991–2023)

Applied to the 33-year Calafat climate record, the model reconstructed annual water stress days over 1991–2023 (Figure 3-19). Mean annual stress was 19.3 days yr^{-1} with a positive trend of +0.09 days yr^{-1}. The distribution is highly skewed: 52% of years recorded zero stress days, but the three worst years were 2011 (109 days), 2012 (83 days), and 1992 (74 days). Mean annual water balance: ETa = 304 mm yr^{-1} and recharge/outflow Q = 249 mm yr^{-1}.

Decade-level analysis reveals a non-monotonic evolution of stress intensity over the 33-year record. The first decade (1991–2000) had the highest mean stress at 22.1 days yr^{-1} and included the severe 1992 drought (74 days); the second decade (2001–2010) was notably milder at 4.3 days yr^{-1} on average; and the most recent period (2011–2023) returned to high stress levels, averaging 28.8 days yr^{-1} and including the most extreme events in the record (2011: 109 days; 2012: 83 days). This pattern is consistent with the SPEI-12 record (Figure 214, Hydrological modelling / monitoring Maglavit/Danube River catchment), which shows the 2000–2001 and 2011–2012 drought episodes as the two most severe periods in the series.

The mean annual water balance (P = 554, ETa = 304, Q = 249 mm yr^{-1}) yields a near-zero long-term storage change (residual 1 mm yr^{-1}), confirming physical consistency of the hindcast. The ETa/P ratio of 0.58 and Q/P ratio of 0.42 are typical of semi-arid continental landscapes with episodic but intense rainfall. Mean daily ETa in the growing season (June–September) is 1.4 mm day^{-1}, compared to 0.5 mm day^{-1} in the dormant season (October–May), reflecting the strong seasonal concentration of water use. In dry years (top 5 by stress days), mean annual ETa declines to approximately 280 mm yr^{-1}, confirming that severe droughts substantially suppress ecosystem water use and by extension primary productivity at the site.

The top panel of Figure 3-19 shows annual mean and minimum root zone SWS alongside annual water stress day counts from 1991 to 2023. The minimum SWS, the annual low point to which the soil is depleted in each year, is the most direct indicator of drought severity: it determines how close the soil reaches the wilting point (WP = 35.3 mm, shown as the dashed reference line) and for how long plants are exposed to water deficit. The Spearman correlation between annual minimum SWS and annual stress days is $r = -0.903$ ($p < 0.001$), confirming that the minimum SWS is the dominant control on stress day count. In 1992, the minimum SWS reached exactly the wilting point (35.3 mm), the most extreme depletion in the record, while 2014 saw a minimum of 92.0 mm, essentially at field capacity, reflecting the exceptional rainfall of that year (979 mm). Most years with zero stress days are characterised by minimum SWS values remaining well above 55 mm throughout the summer, meaning the soil never approached the stress threshold.

The centre-left panel of Figure 3-19 shows annual actual evapotranspiration (ETa) and precipitation over the 33-year record. A modest but statistically significant increasing trend in ETa is visible (+1.2 mm yr^{-1}, $p < 0.001$), driven primarily by the warming temperature trend rather than by changes in water availability. Despite this trend, ETa remains strongly controlled by interannual precipitation variability (Pearson $r = 0.34$), reflecting the water-limited nature of this semi-arid site: in dry years (top 5 by stress days), mean ETa declines to approximately 280 mm yr^{-1}, while in the least stressed years mean ETa is approximately 301 mm yr^{-1} — a difference of only 21 mm because even in wet years the atmospheric demand far exceeds supply. The highest ETa in the record occurred in 2022 (350 mm), a year with high ET_0 demand despite modest precipitation, while the lowest was 1996 (265 mm).

The centre-right panel shows the mean monthly root zone SWS climatology (1991–2023) alongside the monthly frequency of water stress days. This panel reveals the seasonal structure of the water balance: SWS is at or near field capacity from January through June (monthly mean 92–96 mm), begins declining in July, reaches its seasonal minimum in September (mean 75.1 mm, stress frequency 19.2%), and partially recovers through October and November. Stress days are almost entirely confined to July through November: the monthly stress frequency is effectively zero from December to June, rises to 3.3% in July and 16.5% in August, peaks at 19.2% in September, and declines back toward zero by December. The peak stress frequency of 19.2% means that across the 33-year record, roughly one in five Septembers contained at least some water stress days in any given year.

The bottom-left panel of Figure 3-19 shows the full annual distribution of water stress days (1991–2023), with bars coloured red for years above the long-term mean (19.3 days yr^{-1}) and blue for years below. The distribution is strongly right-skewed (skewness = 1.68): the median is zero, the mean is pulled upward by a small number of extreme years. Of the 33 years, 17 (52%) recorded zero stress days, 1 recorded between 1 and 10 days, 8 recorded 11–30 days, 3 recorded 31–60 days, and 4 exceeded 60 days. This bimodal-like pattern reflects the threshold nature of summer drought at this site, once early-season precipitation deficits allow the soil to approach the stress threshold by mid-summer, even small additional deficits produce many stress days, while years with adequate spring recharge are buffered throughout the summer. The positive trend of +0.09 days yr^{-1} is not statistically significant ($p = 0.87$) given the high interannual variability, but the visual pattern in Figure 3 is consistent with the concentration of the most extreme stress events (2011, 2012, 2021) in the most recent decade, alongside the temperature increase identified in the historical climate record.

The bottom-right panel of Figure 3-19 shows the NbS sensitivity curve under baseline climate: mean annual stress days as a function of additional root zone water storage capacity from 0 to +50 mm. The curve is approximately linear in the range explored, with each additional 10 mm of storage reducing mean stress by approximately 3.0–3.9 days yr^{-1}, yielding an overall reduction from 19.3 days at baseline to approximately 3.9 days at +50 mm. Notably, the curve approaches but does not reach zero: even with a 50 mm increase in AWC, a substantial increase representing roughly 80% of the current AWC, some stress years would still occur. This is because the most extreme drought years (2011, 1992, 2000) involve sustained deficits that exceed the additional buffer capacity within a single summer season. The implication is that NbS interventions can eliminate stress in the majority of years but cannot fully insulate the site against compound multi-month droughts, reinforcing the importance of considering NbS effectiveness under both current and future climate conditions.

The bottom heatmap of Figure 3-19 provides the most comprehensive view of how the stress phenology has evolved over the 33-year record. Each row is one year; each column is a day of the year; colour encodes daily SWS (red = depleted, green = at or above field capacity). The consistent green band from January through approximately day 180 (late June) confirms that winter and spring recharge reliably replenishes the profile in all years. The transition to red in late summer is visible in every year, but its timing, depth, and duration vary substantially. The five years with more than 50 stress days, 2011 (109 days), 2012 (83 days), 1992 (74 days), 2000 (71 days), and 2021 (55 days), are clearly identifiable as years with prolonged red bands extending from approximately July through October or November. The heatmap also shows that stress can begin as early as late June in the worst years and that recovery to field capacity can be delayed until December in consecutive drought years such as 2011–2012, when the soil never fully recharged between consecutive summer seasons.

Figure 3-19 Long-term soil water balance model results (1991–2023). Top (full width): annual mean and minimum root zone SWS (green lines, left axis) with annual water stress days (red bars, right axis) for 1991–2023. Centre-left: annual actual ETa (red bars) and precipitation (blue bars) with ETa trend (+1.2 mm yr^{-1}). Centre-right: mean monthly root zone SWS climatology (green line) and monthly stress frequency (red bars) averaged over 1991–2023. Bottom-left: annual water stress days with linear trend (+0.09 days yr^{-1}) and long-term mean (19.3 days yr^{-1}); years above mean in red, below in blue; worst years labelled. Bottom-right: sensitivity under baseline climate — mean annual stress days vs additional root zone water storage capacity (+0 to +50 mm). Bottom (full width): daily root zone SWS heatmap across 33 years (day-of-year on x-axis, year on y-axis; red = depleted, green = at field capacity).

3.4.5 Climate change scenarios and NbS sensitivity

Under the delta-change climate scenarios, mean annual water stress days increase from the baseline (19.3 days yr^{-1}) to 28.5 under RCP4.5 2041–2070, 35.3 under RCP8.5 2041–2070, and 46.6 days yr^{-1} under RCP8.5 2071–2100 (Figure 3-20). The applied delta changes correspond to ET_0 increases of 53, 86, and 151 mm yr^{-1} and precipitation reductions of 23, 46, and 74 mm yr^{-1} respectively (Jacob et al., 2014). Under RCP8.5 2071–2100 the median annual stress is 40 days yr^{-1}, meaning the average year becomes severely stressed.

The NbS sensitivity analysis shows that adding 30 mm of additional root zone water retention capacity halves stress days under current climate: from 19.3 to approximately 9.6 days yr^{-1}. Under RCP8.5 2071–2100, the same intervention reduces stress from 46.6 to approximately 32 days yr^{-1}. These results demonstrate that NbS interventions are most effective under current climate conditions and that early implementation maximises their long-term benefit.

The full NbS sensitivity curves (Figure 3-20, bottom-right) show that under baseline climate, the stress reduction is approximately linear across the range explored: each additional 10 mm of root zone storage capacity reduces mean annual stress days by approximately 3–4 days yr^{-1}, yielding a near-proportional response from 0 to +50 mm. However, the effectiveness of a given intervention diminishes substantially when comparing across climate scenarios: under RCP8.5 2071–2100, a +30 mm addition reduces stress from 46.6 to 32.5 days yr^{-1} (14 fewer days), compared to a reduction of 9.7 days under baseline climate. Even a +50 mm intervention leaves approximately 25 days yr^{-1} of stress under RCP8.5 2071–2100, showing that these imagined NbS cannot offset the full impact of high-end warming.

Practically, a 30 mm increase in root zone water storage capacity is achievable through several interventions at the Maglavit–Cetate site. Partial reconnection of the former fish ponds to seasonal Danube flood pulses would periodically recharge soil profiles to depths well below 45 cm. Shallow retention micro-dams could intercept surface runoff during high-intensity autumn events, such as the 105 mm event of 2–3 October 2025, and allow extended infiltration. Soil organic matter improvement through cover cropping or biochar amendment on the arable portions of the site could directly raise field capacity and AWC. The quantitative framework established here provides the evidence base to design, prioritise, and monitor the hydrological effectiveness of such interventions over time.

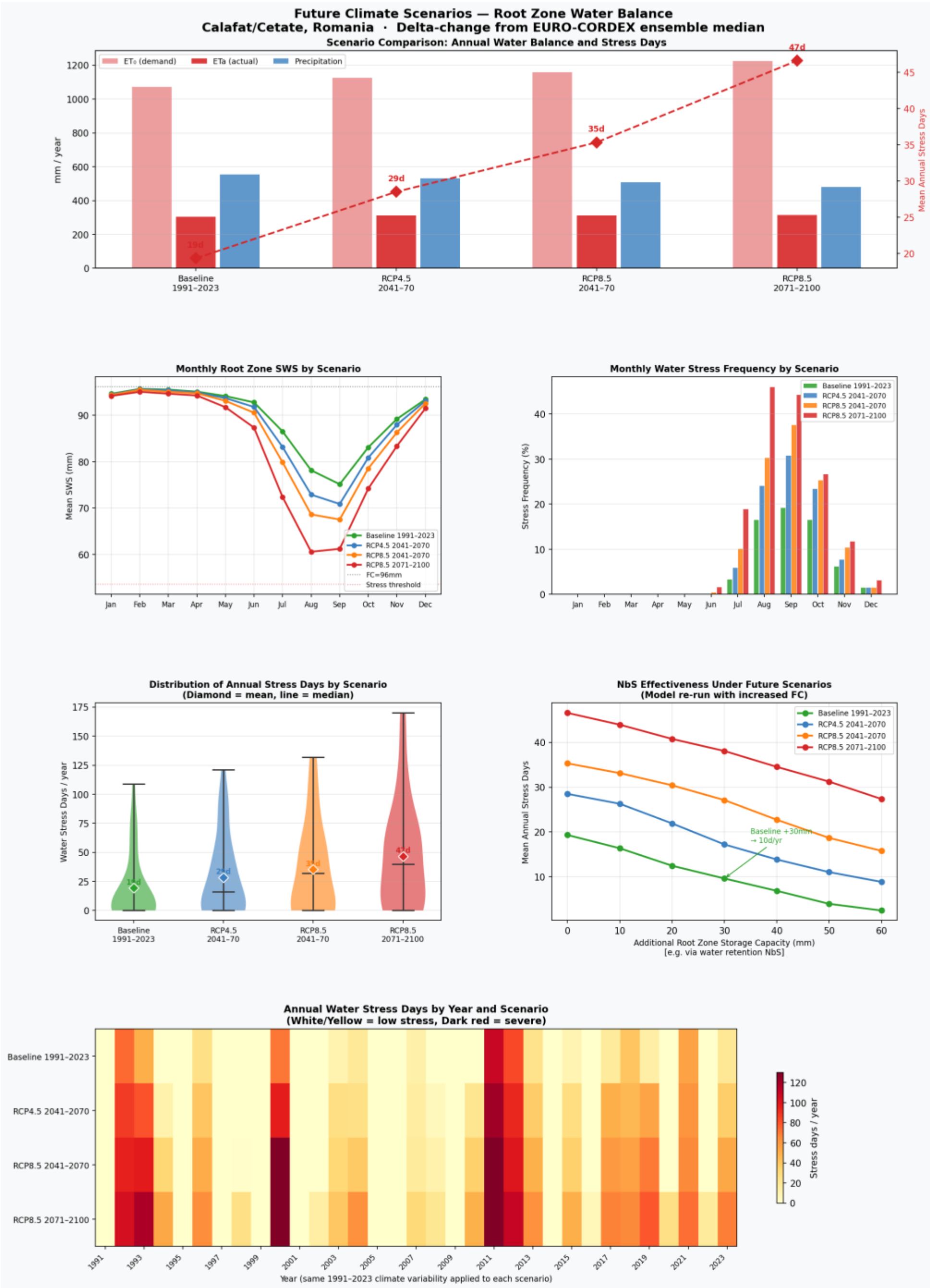

Figure 3-20 Climate change scenario analysis and NbS sensitivity (EURO-CORDEX delta-change, four scenarios). Top (full width): annual water balance by scenario — ET_0 demand (light red), actual ETa (dark red), and precipitation (blue) as bars; mean annual stress days as diamonds on secondary axis. Centre-left: mean monthly root zone SWS by scenario with stress threshold indicated. Centre-right: monthly water stress frequency by scenario (grouped bars). Bottom-left: distribution of annual stress days by scenario (violin plots; diamond = mean, horizontal line = median). Bottom-right: effectiveness — mean annual stress days vs additional root zone storage capacity (+0 to +60 mm) for all four scenarios. Bottom (full width): annual water stress days by year and scenario (heatmap; white/yellow = low stress, dark red = severe).

4 Conclusions

4.1 AT- Liesingbach Living Lab

The importance of vegetation in moderating peak water temperatures has been clearly demonstrated for the river Liesingbach. Its ecological value for maintaining water quality is immense, it strongly supports the ecological flow during low flow situations. Differences of 4.9°C between different shading scenarios in peak water temperatures can have major ecological consequences for riparian systems. In the critical range of temperatures above 20°C, even small temperature changes can alter habitat suitability e.g. for fish, as many species exhibit narrow thermal tolerance zones.

Based on our results, vegetation effects are not limited to dense riparian forests. Even single tree lines, or shrubby vegetation implemented through slow hydrology techniques in the riparian corridor have remarkable influence on water temperature. Vegetation can clearly support ecological aspects during low flows. With the prevailing water temperature model, we created a tool to quantify the impacts and predict potential changes. Building on this integration of hydraulic and vegetation modelling will enable us to improve ecological outcomes during low-flow periods.

4.2 DK- Vaerebro Living Lab

The preliminary results from the Værebro Living lab, show that the Værebro submodel, based on DK-model2026, demonstrates an overall acceptable performance when evaluated against national-scale criteria. The model is used to evaluate key hydrological characteristics of the catchment, including seasonal variations in evapotranspiration, discharge, and groundwater levels. Generally, there is a high spatial variance across subcatchments, highlighting the influence of upstream and downstream processes. Groundwater levels show significant variability, especially during dry periods, reflecting the heterogeneity of the catchment. Five different scenarios (two slow hydrology and three anthropogenic/water management scenarios) were tested in the model. The scenario analyses reveal that no single intervention effectively mitigates both drought and flooding conditions. Reducing abstraction improves low-flow conditions in streams but has a limited impact on groundwater drought. In contrast, removing drainage significantly raises groundwater levels during the dry season, but at the same time negatively impacts the dry flow indicators in the stream. Overall, there is a need to further investigate slow hydrology solutions, especially their different spatial impacts in the subcatchments, as well as their potential effect in a changing climate.

4.3 RO-Maglavit Living Lab

Preliminary results from the Romanian Living Lab indicate a site characterised by severe and structurally persistent summer water deficits, with mean annual ET_0 exceeding precipitation by approximately 519 mm yr^{-1} and a statistically significant warming-driven increase in atmospheric demand of +40 mm $decade^{-1}$ over the 1991–2023 period, while precipitation shows no significant trend. Monitoring data from June 2025 to January 2026 confirm the expected soil moisture dynamics: the root zone desiccated to near wilting point by late September 2025 (SWS approximately 31 mm), with summer rainfall events failing to penetrate below 30 cm in all six cases observed, while 10 of 11 autumn and winter events readily recharged the profile to 45 cm or deeper. A key finding is that antecedent atmospheric demand, rather than event rainfall alone, is the dominant control on infiltration depth (Spearman $r = -0.740$, $p = 0.001$), which has direct implications for the timing and effectiveness of NbS interventions. The 33-year hindcast shows that water stress at this site is episodic rather than chronic, with 52% of years recording zero stress days and a long-term mean of 19.3 days yr^{-1}, but stress intensity is variable across decades: the 2001–2010 period was unusually mild (4.3 days yr^{-1}), while the most recent period (2011–2023) is the most stressed on record at 28.8 days yr^{-1}, consistent with the rising ET_0 trend. Sensitivity analysis indicates that a modest increase of 30 mm in root zone water retention capacity, achievable through targeted NbS measures, would approximately halve current mean annual stress days from 19.3 to 9.6, though this benefit diminishes substantially under high-end warming scenarios, underlining the importance of early implementation.

4.4 PT-Toutalga Living Lab

Being the Toutalga a predominantly natural basin with a non-modified hydrological regime its reasonable to consider and strategically advantageous to implement a hydro-environmental monitoring system as part of a pilot or demonstrator. Coupling continuous data acquisition with hydrological modelling deepens the understanding of flood dynamics and other environmental impacts by providing real-time feedback, improving model calibration, and capturing natural variability with high fidelity. Effects on hydrology, water quality, and ecosystem resilience can be directly monitored and quantified. Modeling water detention solutions as part of flood protection strategies in urban environments can significantly increase community resilience; moreover, by temporarily storing surface runoff, it can simultaneously contribute to ecological stability.

Furthermore, the basin provides an ideal testbed for the integration of Nature-Based Solutions (NBS), which can be deployed to enhance the outcomes already achieved.

5 References

Allen, R.G., Pereira, L.S., Raes, D., Smith, M. (1998). Crop evapotranspiration — Guidelines for computing crop water requirements. FAO Irrigation and Drainage Paper 56. FAO, Rome.

Botter, G., Porporato, A., Rodriguez-Iturbe, I., & Rinaldo, A. (2007). Basin-scale soil moisture dynamics and the probabilistic characterization of carrier hydrologic flows: Slow, leaching-prone components of the hydrologic response. *Water Resources Research*, *43*(2), 2006WR005043. https://doi.org/10.1029/2006WR005043

Brunner, G. W. 2016. "HEC-RAS River Analysis System User's Manual." US Army Corps of Engineers, Institute for Water REsources Hydrologic Engnineering Center (HEC), 609 Second Street, Davis, CA.

Christine, P., Jerzy, S., Hanna, W., & Krzysztof, R. (2005). Dynamic slowdown: A flood mitigation strategy complying with the integrated management concept – implementation in a small mountainous catchment. *International Journal of River Basin Management*, *3*(2), 75–85. https://doi.org/10.1080/15715124.2005.9635247

Delta-T Devices Ltd. (1999) "HemiView." Cambridge, UK. Available at: https://hemiview.software.informer.com/ (Accessed: April 2, 2026).

D. N. Moriasi *et al.* (2007) "Model Evaluation Guidelines for Systematic Quantification of Accuracy in Watershed Simulations," *Transactions of the ASABE*, 50(3), pp. 885–900. Available at: https://doi.org/10.13031/2013.23153.

Engineers, Institute for Water REsources Hydrologic Engnineering Center (HEC), 609 Second Street, Davis, CA.Falkenmark, M., & Wang-Erlandsson, L. (2021). A water-function-based framework for understanding and governing water resilience in the Anthropocene. *One Earth*, *4*(2), 213–225. https://doi.org/10.1016/j.oneear.2021.01.009

Fluet-Chouinard, E., Stocker, B. D., Zhang, Z., Malhotra, A., Melton, J. R., Poulter, B., Kaplan, J. O., Goldewijk, K. K., Siebert, S., Minayeva, T., Hugelius, G., Joosten, H., Barthelmes, A., Prigent, C., Aires, F., Hoyt, A. M., Davidson, N., Finlayson, C. M., Lehner, B., ... McIntyre, P. B. (2023). Extensive global wetland loss over the past three centuries. *Nature*, *614*(7947), 281–286. https://doi.org/10.1038/s41586-022-05572-6

GeoSphere Austria (2024) "Messstationen Stundendaten v2." Available at: https://doi.org/10.60669/9bdm-yq93.

Gies, E. (2022). *Water always wins: Thriving in an age of drought and deluge*. The University of Chicago Press.

Granata, F., & Di Nunno, F. (2025). Pathways for Hydrological Resilience: Strategies for Adaptation in a Changing Climate. *Earth Systems and Environment*. https://doi.org/10.1007/s41748-024-00567-x

Harder, P., Pomeroy, J. W., & Westbrook, C. J. (2015). Hydrological resilience of a Canadian Rockies headwaters basin subject to changing climate, extreme weather, and forest management. *Hydrological Processes*, *29*(18), 3905–3924. https://doi.org/10.1002/hyp.10596

Harvey, J. W. (2016). Hydrologic Exchange Flows and Their Ecological Consequences in River Corridors. In *Stream Ecosystems in a Changing Environment* (pp. 1–83). Elsevier. https://doi.org/10.1016/B978-0-12-405890-3.00001-4

Haubrock, P. J., Stubbington, R., Fohrer, N., Hollert, H., Jähnig, S. C., Merz, B., Pahl-Wostl, C., Schüttrumpf, H., Tetzlaff, D., Wesche, K., Tockner, K., & Haase, P. (2025). A Holistic Catchment-Scale Framework to Guide Flood and Drought Mitigation Towards Improved Biodiversity Conservation and Human Wellbeing. *WIREs Water*, *12*(1), e70001. https://doi.org/10.1002/wat2.70001

Jaafar, H.H., Ahmad, F.A. & El Beyrouthy, N. (2019). GCN250, new global gridded curve numbers for hydrologic modeling and design. Sci Data 6, 145. https://doi.org/10.1038/s41597-019-0155-x

Jacob, D. et al. (2014). EURO-CORDEX: new high-resolution climate change projections for European impact research. Regional Environmental Change, 14(2), 563–578.

McKee, T.B., Doesken, N.J., Kleist, J. (1993). The relationship of drought frequency and duration to time scales. 8th Conference on Applied Climatology, AMS, 179–183.

Nislow, K. H., Magilligan, F. J., Saleeba, M., & Palmer, R. E. (2024). Slowing the flow for climate resilience in human-dominated riverine landscapes. In *Resilience and Riverine Landscapes* (pp. 545–568). Elsevier. https://doi.org/10.1016/B978-0-323-91716-2.00002-9

Rich, P.M. *et al.* (1999) "HemiView Manual Revision Number: 2.1." Delta-T Devices Ltd, 130 Low Road, Burwell, Cambridge, UK.

Rolls, R. J., Leigh, C., & Sheldon, F. (2012). Mechanistic effects of low-flow hydrology on riverine ecosystems: Ecological principles and consequences of alteration. *Freshwater Science*, *31*(4), 1163–1186. https://doi.org/10.1899/12-002.1

Stonewall, A.J. and Buccola, N.L. (2015) *Development of a HEC-RAS temperature model for the North Santiam River, northwestern Oregon*. Open-File Report. U.S. Geological Survey, Reston, Virgina. Available at: https://doi.org/10.3133/ofr20151006.

UNESCO & WMO (Eds.). (2012). *International glossary of hydrology: = Glossaire international d'hydrologie*. WMO.

Vicente-Serrano, S.M., Beguía, S., López-Moreno, J.I. (2010). A multiscalar drought index sensitive to global warming: the SPEI. Journal of Climate, 23(7), 1696–1718.

Zhang, Z. and Johnson, B.E. (2017) “Hydrologic Engineering Center-River Analysis System (HEC-RAS) Water Temperature Models Developed for the Missouri River Recovery Management Plan and Environmental Impact Statement.” U.S. Army Corps of Engineers Washington, DC 20314-1000.

End of document